

On the radiation environment during consecutive balloon flights over New Mexico and Antarctica

Thomas Berger¹, Daniel Matthiä¹, Karel Marsalek¹, Bartos Przybyla¹, Joachim Aeckerlein¹, Markus Rohde¹, Michael Wirtz¹, Ralf Moeller¹, Leandro M. James², Michael A. Lane², Prital Johnson², Brian F. Rauch³, Marianne B. Sowa², and David J. Smith²

¹German Aerospace Center

²NASA

³Washington University

November 23, 2022

Abstract

Remarkably, we know more about the radiation environment onboard the International Space Station than we do about radiation values at altitudes between 30-40 km in the middle stratosphere. Within this work, we provide data about the radiation dose measured during two consecutive balloon flights flown within a 4-month timeframe over New Mexico and Antarctica. Data were measured with the M-42 radiation detector. On each flight, the M-42 was installed as part of a larger research payload: MARSBOx (New Mexico, 23 September 2019); and E-MIST (Antarctica, 15 December 2019-12 January 2020). The temporal proximity of the flights provided similar prevailing space weather conditions and solar activity (minimal during each mission). Against that common backdrop, the main differences between flights, including mission duration and geomagnetic shielding could be readily compared. Near identical space weather conditions provided a window of opportunity for studying the influence of altitude and geomagnetic shielding on dose and fluence rate of galactic cosmic radiation under maximum intensity conditions. Herein, we report relevant count- and dose rates for the missions, alongside Geant4 Monte Carlo calculations; this included crossings of the Regener maximum during the ascent and descent flights over New Mexico and the absence of a distinct maximum in dose rates at zero geomagnetic shielding for the polar flight. While dose rates in silicon at float altitudes (35 km-39 km) were a maximum of 2.5 ± 0.4 microGy/h over New Mexico, we reached values of up to 8.4 ± 0.3 microGy/h over Antarctica, thereby approaching dose rates similar to the surface of Mars.

1 On the radiation environment during consecutive balloon flights over New Mexico 2 and Antarctica

3 Thomas Berger¹, Daniel Matthiä¹, Karel Marsalek¹, Bartos Przybyla¹, Joachim
4 Aeckerlein¹, Markus Rohde¹, Michael Wirtz¹, Ralf Moeller¹, Leandro M. James², Michael
5 A. Lane², Prital J. Johnson², Brian F. Rauch³, Marianne B. Sowa⁴, David J. Smith⁴

6 ¹German Aerospace Center (DLR), Institute of Aerospace Medicine, Cologne, Germany

7 ²NASA Kennedy Space Center, Engineering Directorate, FL, USA

8 ³Department of Physics and McDonnell Center for the Space Sciences, Washington University in
9 St. Louis, MO, USA

10 ⁴NASA Ames Research Center, Space Biosciences Division, CA, USA

11
12 Corresponding author: Thomas Berger (thomas.berger@dlr.de)

13 Key Points:

- 14 • Radiation dose values, fluence and energy distribution spectra were measured for two
15 distinct stratospheric balloon flights
- 16 • Long duration balloon flight observations occurred over New Mexico (7 hours) and over
17 Antarctica (28 days)
- 18 • The Regener maximum was identified and described for both missions

19 Abstract

20 Remarkably, we know more about the radiation environment onboard the International
21 Space Station than we do about radiation values at altitudes between 30-40 km in the middle
22 stratosphere. Within this work, we provide data about the radiation dose measured during two
23 consecutive balloon flights flown within a 4-month timeframe over New Mexico and Antarctica.
24 Data were measured with the M-42 radiation detector. On each flight, the M-42 was installed as
25 part of a larger research payload: MARSBOx (New Mexico, 23 September 2019); and E-MIST
26 (Antarctica, 15 December 2019-12 January 2020). The temporal proximity of the flights
27 provided similar prevailing space weather conditions and solar activity (minimal during each
28 mission). Against that common backdrop, the main differences between flights, including
29 mission duration and geomagnetic shielding could be readily compared. Near identical space
30 weather conditions provided a window of opportunity for studying the influence of altitude and
31 geomagnetic shielding on dose and fluence rate of galactic cosmic radiation under maximum
32 intensity conditions. Herein, we report relevant count- and dose rates for the missions, alongside
33 Geant4 Monte Carlo calculations; this included crossings of the Regener maximum during the
34 ascent and descent flights over New Mexico and the absence of a distinct maximum in dose rates
35 at zero geomagnetic shielding for the polar flight. While dose rates in silicon at float altitudes
36 (≈ 35 km-39 km) were a maximum of 2.5 ± 0.4 $\mu\text{Gy/h}$ over New Mexico, we reached values of up
37 to 8.4 ± 0.3 $\mu\text{Gy/h}$ over Antarctica, thereby approaching dose rates similar to the surface of Mars.

40 Plain Language Summary

41 The radiation environment during two high altitude balloon missions was measured with
42 the German Aerospace Center M-42 radiation detector. These missions were successfully
43 executed in September 2019 over New Mexico (MARSBOx) and in December 2019 and January
44 2020 over Antarctica (E-MIST) with a collaboration between NASA and DLR. Considering the
45 missions were flown at similar, near solar minimum conditions, we could readily draw
46 comparisons of the radiation environment at two distinct locations in Earth's middle stratosphere
47 (polar and mid-latitude profiles).

48 1. Introduction

49 The Space radiation environment has been extensively studied, even at inaccessible
50 locations, including at high altitudes where aircraft travel, in low Earth orbit (LEO) onboard the
51 International Space Station (ISS) (Berger et al., 2020), and, more recently, on the surface of other
52 planetary bodies such as the Moon (Zhang et al., 2020) and Mars (Zeitlin et al., 2019; Berger et
53 al., 2020). The components of the radiation environment in deep space result from galactic
54 cosmic radiation (GCR) and sporadic solar particle events (SPEs). However, when considering
55 the radiation environment at LEO altitudes – applicable to a spacecraft like the ISS – charged
56 particles trapped inside the radiation belts must also be accounted for in measurements and
57 models. Due to mass shielding (effective against the electrons in the outer radiation belt), the
58 most relevant radiation belt contribution to the radiation exposure of astronauts inside the ISS is
59 derived from trapped protons in the South Atlantic Anomaly (SAA). Measuring radiation doses
60 for commercial aircraft traveling through the tropopause/lower stratosphere (~10 km – 12 km) is
61 a similarly complex exercise due to GCR scattering into the atmosphere, creating a mixed
62 radiation field of primary and secondary particles (with a high contribution from electrons and
63 neutrons). Due to numerous radiation measurements in the regions where commercial aircraft
64 and human spacecraft regularly travel, these environments can now be quite reliably
65 characterized and described. Yet the same is not true for a wide zone of our Earth's middle
66 stratosphere, around 20 – 40 km, which to this day remains essentially uncharted territory for
67 fundamental dose rate measurements. To date, information characterizing the radiation field in
68 this region of the atmosphere has been built upon only a handful of scientific balloon
69 measurements.

70 Considering exposure to GCR is a major, unresolved risk for human spaceflight, we note
71 the potential utility of using the Earth's stratosphere for establishing a natural testbed to study the
72 influence of mass and geomagnetic shielding on dose. For instance, shielding conditions in space
73 cannot be realistically changed to perform such systematic studies, but changing altitude
74 (air pressure) during a balloon flight into the stratosphere can quantify the mass shielding
75 parameter quite precisely. Measurements on balloons introduce atmospheric shielding between
76 approximately 1000 g/cm² and a few g/cm². If utilizing the full range of the dynamic proxy,
77 teams could conceivably draw comparisons with conditions encountered in a spacecraft like the
78 ISS (i.e., lowest mass shielding); or conditions expected on other planets with comparable
79 atmospheric densities (i.e., higher mass shielding). Thus, additional data from the Earth's
80 stratosphere will be valuable for benchmarking models that calculate the exposure from cosmic
81 radiation for a variety of imminent space exploration scenarios. In the 1930s it was discovered
82 that the intensity of primary and secondary particles of cosmic radiation as measured by
83 ionization rates at a given altitude can go through a maximum (Regener & Pfozter, 1935). Based

84 on the work by Carlson & Watson (2014), this ionization phenomenon, is now denoted as the
85 *Regener-maximum*, and the altitude where the maximum occurs depends on the specific
86 boundary conditions.

87 In the decades following this discovery, the ionization rates in the atmosphere were
88 studied extensively as a function of altitude (Carmichael & Dymond, 1939; Lowder & Beck,
89 1966; Lowder et al., 1972; Neher, 1958, 1971; Rosen et al., 1985). The variation of these profiles
90 caused by solar modulation at high geomagnetic latitudes was comprehensively investigated by
91 Neher (1971) and it was shown that the ionization rate did not form a maximum at high latitudes
92 during solar minimum conditions. Later, detailed studies of individual particle species followed,
93 such as electrons (Boezio et al., 2000; DuVernois et al., 2001), protons and helium (Bellotti et
94 al., 1999; Boezio et al., 1999), and neutrons (Goldhagen et al., 2004). An overview of historical
95 measurements was compiled by Grieder (2001); in short, many of the past studies focused on
96 primary GCR spectra and their properties but did not systematically investigate the development
97 of the radiation field in the atmosphere. Unfortunately, to date, stratospheric radiation data
98 remain sparse, especially for the case of low or zero geomagnetic shielding parameters; scenarios
99 particularly relevant for the full GCR field in interplanetary space or on planets without magnetic
100 fields. To our knowledge, no dose rate measurements at zero geomagnetic shielding and very
101 low atmospheric shielding levels exist in literature for balloon-flown experiments. Recent
102 radiation measurements at intermediate geomagnetic shielding conditions were made on a
103 balloon flight up to 36 km by the NASA Radiation Dosimetry Experiment (RaD-X) campaign
104 (Mertens, 2016; Mertens et al., 2016; Straume et al., 2016; Hands et al., 2016; Norman et al.,
105 2016), with one emphasis of this previous investigation was drawing comparisons with
106 concurrently-flown aircraft at lower altitudes (11 km) (Meier et al., 2016). With such predecessor
107 missions squarely in mind, we aimed to continue expanding knowledge about the radiation
108 conditions in the middle stratosphere by acquiring new measurements on consecutively-flown
109 balloon missions at mid- and polar latitudes. Our first experiment was over New Mexico
110 (resembling the RaD-X campaign flight profile) in September 2019 onboard the NASA Microbes
111 in Atmosphere for Radiation, Survival, and Biological Outcomes Experiment (MARSBOx)
112 payload (Cortese et al., 2021). This was supplemented by another flight opportunity over
113 Antarctica launched in December 2019 onboard the NASA Exposing Microorganisms in the
114 Stratosphere (E-MIST) payload (Smith et al., 2014), which was carried by the Super Trans-Iron
115 Galactic Element Recorder (Binns et al., 2013; Hams et al., 2016; Rauch et al., 2019)
116 (SuperTIGER)-2.3 mission on a 32-day polar mission that circumnavigated the continent twice.
117 Our measurements captured dose rate profiles in the stratosphere over a wide range of
118 atmospheric shielding (under comparable atmospheric conditions) and for maximum GCR
119 intensity but with different geomagnetic shielding. Taken together, our unique datasets can be
120 compared to model calculations, providing detailed insights into the composition of the middle
121 stratosphere radiation field and the contribution of different particles to the dose rates.

122 **2. Instrumentation and stratospheric balloon flights**

123 This study will provide data to describe the radiation environment measured with the
124 DLR M-42 radiation detector (Berger et al., 2019) onboard two scientific balloon experiments
125 carried out in collaboration with NASA. The high-altitude balloon flights were performed first
126 over New Mexico (MARSBOx experiment) and next over Antarctica (E-MIST experiment).
127 First, we will provide an overview of the radiation detector instrument (section 2.1) followed by

128 an overview of the space weather conditions (section 2.2). After establishing that background,
 129 we provide a description of the MARSBOx and the E-MIST experiments (section 2.3 and 2.4).

130 2.1 The M-42 instruments for MARSBOx and E-MIST

131 DLR developed the M-42 radiation detector family (Berger et al., 2019) to have a small,
 132 easy-to-use and easy-to-adjust radiation measurement system, adjustable to various payload
 133 configurations and robust enough to travel to extreme environments including the upper
 134 atmosphere. The M-42 detector is based on one silicon diode with a thickness of 300 μm and an
 135 active area of 1.22 cm^2 . This configuration enables the measurements of the energy deposition
 136 (E_{Dep}) spectra in Si from 0.07 to 20 MeV and the determination of the absorbed dose in Si.
 137 Instrument power can come from Li primary or Li-ion rechargeable batteries, or from a
 138 micro-USB connector for longer duration flights. For our two balloon missions, version
 139 M-42_Compact (M-42_C) of the radiation detector was flown (see Figure 2 in Berger et al.,
 140 2019). Hereafter for simplicity, the M-42_C instrument will be denoted as M-42. Table 1
 141 provides the flight details and the dosimeter acquisition specifications. Prior to each balloon
 142 flight, the M-42 instruments were integrated into the NASA payload compartments and
 143 connected via micro-USB cable to the dedicated power outlets (see further information in section
 144 2.3 for MARSBOx and in section 2.4 for E-MIST).

145 The measurements were initiated upon balloon launch by providing power to the device
 146 approximately 5 min after launch. For the shorter duration MARSBOx mission (~7 hours), a
 147 5 min integration time for the energy deposition spectra was used. In comparison, for the longer
 148 duration E-MIST mission (~28 days), radiation data were stored every 30 minutes in the
 149 non-volatile flash memory of the instrument. Readout of the M-42 dosimeters was performed
 150 upon return to DLR following the balloon missions. Prior to the September 2019 MARSBOx
 151 flight, the M-42 was shipped to NASA in July 2019; after the flight the M-42 was returned to
 152 DLR in November 2019. For MARSBOx, a total number of 86 data files were stored resulting in
 153 7 hours 10 min of experimental data. Prior to the E-MIST polar flight the M-42 unit was
 154 provided to NASA in July 2019; after the E-MIST payload returned from Antarctica, the M-42
 155 was transported back to the DLR in May 2020. For E-MIST, a total number of 1346 data files
 156 were stored resulting in 673 hours of experimental data.
 157

158 Table 1

159 *MARSBOx and E-MIST: space weather conditions and M-42 setup*

	MARSBOx	E-MIST
Location	Ft. Sumner, New Mexico	Antarctica
Date	23 Sept. 2019	15 Dec. 2019 - 21 Jan. 2020
Sunspot number	1.1 \pm 0.3 (Sept. 2019)	1.5 \pm 0.5 (Dec. 2019) 6.2 \pm 0.7 (Jan. 2020)
Oulu NM (Cts/min)	6749	6748
R_C (GV)	3.95	0 - 1.4
Part Number (P/N)	001	003
Power	micro-USB	
Measurement duration	23.09.2019 14:05:33 – 21:15:33	15.12.2019 13:55:35 – 12.01.2020 14:55:35
Integration intervall (min)	5	30
Data storage	Non-volatile flash memory	
Data files (#)	86	1346
Data duration	7 h 10 min	28 d 1 h

2.2 Space weather conditions during MARSBOx and E-MIST missions

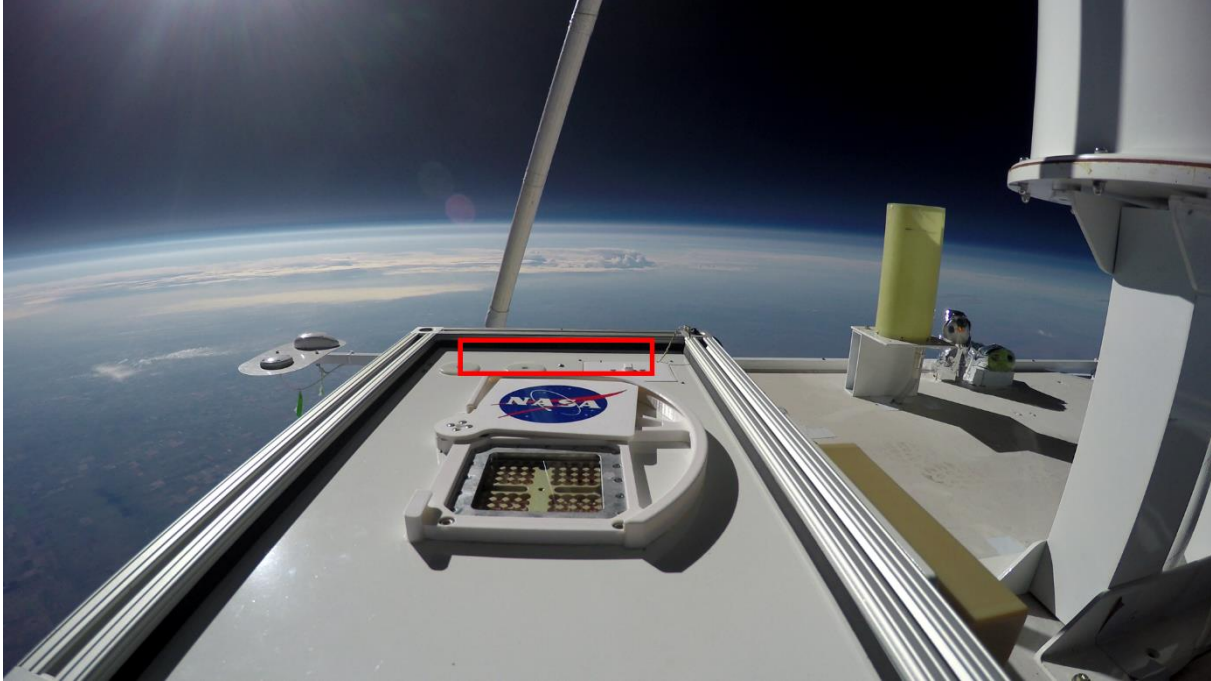
Both balloon flights occurred during the solar minimum between solar cycle 24 and solar cycle 25 under extremely quiet space weather conditions. The monthly mean sunspot number (obtained from <http://www.sidc.be/silso/>) was very low in September 2019 (1.1 ± 0.3), in December 2019 (1.5 ± 0.5) and in January 2020 (6.2 ± 0.7) (see Table 1). At the time of our measurements, the GCR intensity was near its maximum and comparable to the peak values from the previous solar minimum in 2009 which had reached values unprecedented since the beginning of direct GCR intensity measurements. GCR intensity as measured by Neutron Monitors (NM) was similar during the measurements acquired in New Mexico and Antarctica: e.g. Oulu NM count rate (obtained from <https://cosmicrays oulu.fi/>) was 6749 cts/min during the MARSBOx flight (average over 2019-09-23 00:00 UTC to 2019-09-24 00:00 UTC) and 6748 cts/min during the E-MIST campaign (average over 2019-12-15 00:00 UTC to 2020-01-17 00:00 UTC). Also, across our measurements in both locations, variations in the 10 min averages of the NM count rates from the average over the full period were below 2%, showing roughly constant GCR intensities.

Geomagnetic conditions were stable for both balloon flights, as well. The Kp index (<ftp://ftp.gfz-potsdam.de/pub/home/obs/kp-ap/>) reached a maximum value of 1+ during the MARSBOx flight and stayed well below 3 for most of the E-MIST mission with short periods of minor disturbances ($Kp\leq 4$) which did not affect the measurements significantly. The short periods of slightly higher disturbances on 18 December 2019, 6 and 10 January 2020 were caused by faster solar wind streams (bulk speed up to 550 km/s measured by ACE SWEPAM, <ftp://ftp.swpc.noaa.gov/pub/lists/ace/>) had no distinct effect on GCR intensity. In summary, background GCR intensities during the measurements acquired over New Mexico and Antarctica were effectively identical and the geomagnetic field can be characterized as undisturbed. However, the main difference for the two flight campaigns was the geomagnetic cut-off rigidity (R_C). While this was approximately constant ($R_C = 3.95$ GV) for the flight over New Mexico, it varied from $R_C = 0$ GV to 1.4 GV for the Antarctic mission, thereby enabling the comparison of data measured at similar solar conditions but distinct geomagnetic shielding (see further section 3).

2.3 MARSBOx

A complete hardware description of the MARSBOx payload was described elsewhere (Cortês et al., 2020). The dimensions of the payload were 38.1 cm x 25.4 cm x 63.5 cm with a mass of 18 kg that included a 14.8V, 25.2Ah lithium-ion polymer battery (CU-J141, BatterySpace). The payload was designed to also receive a direct connection to other power sources from a balloon gondola (input range of 9V - 36V) but, due to the short duration of the New Mexico flight, an external battery was used to allow for simpler integration. The M-42 dosimeter was housed in an unpressurized container framed from T-slotted 80/20 aluminum extrusions with white powder-coated aluminum panels to reduce solar heating at float altitudes. Commanding the M-42 and other MARSBOx payload instruments was done through a control panel that had light emitting diodes (LEDs) for indicating system readiness for the onboard computer (OSD3358, Octavo Systems) GPS receiver (GPS_FGPMMPA6H, Adafruit Industries), camera system (Hero4 Black, GOPRO with Dash controller, CamDo), and heater system. On 23 September 2019 at 14:00 UTC, the MARSBOx payload was launched from Ft. Sumner, New Mexico, USA (latitude: 34.49° longitude: -104.2°) for a mission (LDB #697NT) lasting approximately 7.5 hours; ~ 4 hours were at the float altitude of ~ 38 km. The M-42 dosimeter was activated 5

205 minutes into the launch (at 14:05 UTC) when the balloon was at 3.07 km. At 21:19 UTC on
 206 descent at 1.75 km, the M-42 was turned off prior to the gondola with MARSBOx landing at a
 207 location northwest of Ft. Sumner (latitude: 35.29° longitude: -105.1°). Figure 1 shows the
 208 MARSBOx experiment over New Mexico with a view looking over the horizon. The M-42 was
 209 positioned beneath the *red box* indicated in Figure 1.
 210



211
 212
 213 Figure 1. MARSBOx at float altitude (~38 km) over New Mexico, looking out at horizon. The
 214 location of M-42 is depicted by superimposed *red box*. © NASA

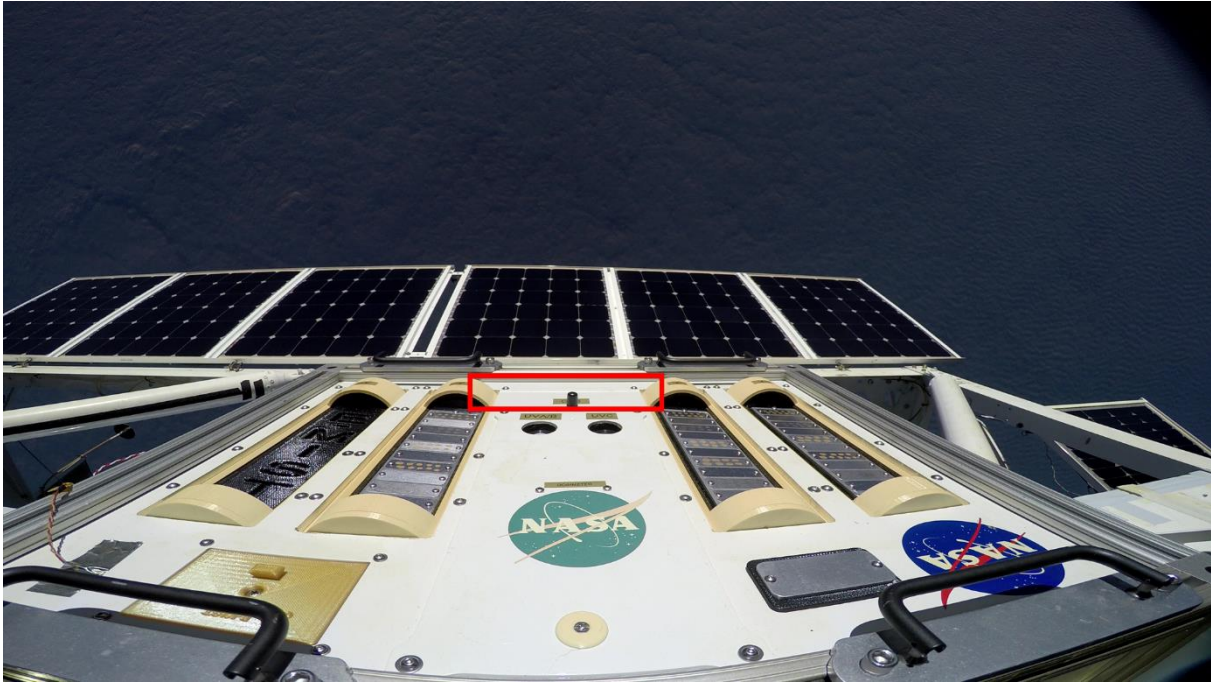
215 2.4 E-MIST

216 Hardware specifications E-MIST payload can be found elsewhere (Smith et al., 2014;
 217 Khodadad et al., 2017). After sea vessel transportation to New Zealand in October 2019, the
 218 E-MIST payload was flown to McMurdo Station, Antarctica, and mounted onto the sunlit side
 219 of the SuperTIGER-2.3 balloon gondola (Rauch et al., 2019) in December 2019 (see Figure A1)
 220 at the Long Duration Balloon (LDB) site on ice outside of McMurdo Station for flight LDB
 221 #706N. The M-42 dosimeter and other instruments were housed inside the unpressurized E-
 222 MIST payload container built from white powder coated aluminum panels and T-slotted 80/20
 223 aluminum framing. System power was provided by a direct connection to the SuperTIGER-2.3
 224 photovoltaic array. During pre-launch time on the Antarctic ice, E-MIST payload components
 225 were kept warm by using 8.5 W heating pads (Omegalux Kapton Insulated Flexible Heater,
 226 Omega). The payload's avionics system (chipKIT Max32, Digilent) recorded data onto a micro-
 227 SD card (BOB-00544, microSD Transflash Breakout, SparkFun), including flight imagery
 228 (Hero4 Black, GOPRO with Dash controller, CamDo). Payload commands were derived from an
 229 onboard altimeter (MS5607, Parallax). A GPS unit (SPK-GPS-GS407A, S.P.K. Electronics Co.)
 230 recorded position data throughout the mission.

231 The 32-day mission was launched on 15 December 2019 at 13:55 UTC and carried into
 232 the stratosphere by a 39.5 million-cubic-foot balloon system. Once at float, the balloon altitude

233 ranged between 33.5 km to 39.3 km, due to periodic thermal conditions. After two full
 234 circumnavigations of the continent, each lasting approximately 16 days, the mission concluded
 235 and touched down on the ice shelf. The gondola landed about 787 km southeast of McMurdo
 236 Station on flat, snow-covered terrain, 2.02 km above sea level (latitude: -71.1255° , longitude:
 237 158.585°) and the E-MIST payload was recovered by a field team on 21 January 2020 (see
 238 Figure A2). Figure 2 shows the E-MIST payload over Antarctica with a viewing direction
 239 looking downward toward the ice shelf. The M-42 was positioned beneath the *red box* indicated
 240 in Figure 2.

241



242

243

244 Figure 2. E-MIST at float altitude over Antarctica (~ 36 km), looking down on the cloud cover
 245 below. The location of M-42 is depicted by superimposed *red box*. © NASA

246 3. Geant4 Simulations

247 Experimental data taken during the balloon flights were used to validate model
 248 calculations of the radiation field in the atmosphere for each location. This approach was
 249 particularly important due to the scarcity of dose measurements at altitudes higher than
 250 commercial air flights (above about 12 km). The flights were performed at similarly low solar
 251 modulation and correspondingly high GCR intensities. Therefore, we could directly compare: (1)
 252 model and measurement agreement or disagreement; and (2) dose rate profiles at low
 253 geomagnetic shielding in Antarctica and at higher geomagnetic shielding in New Mexico.
 254 Furthermore, comprehensive information on composition and energy dependence of the
 255 corresponding particle spectra provided by model calculations could be applied towards a better
 256 understanding of the radiation field.

257 In order to perform the model calculations associated to the measurements, the
 258 experimental conditions must be reproduced. The most important parameters, apart from altitude,
 259 would be geomagnetic shielding quantified by the effective vertical cut-off rigidity R_C and solar
 260 modulation. While the latter was almost identical during the two measurement campaigns on

261 23 September 2019 and between December 2019 and January 2020, R_C differed significantly.
 262 While the cut-off rigidity was treated as approximately constant ($R_C = 3.95$ GV) for the one-day
 263 measurement in New Mexico, the variations over the weeks long flight over Antarctica ($R_C =$
 264 0 GV to 1.4 GV) had to be considered in the model (Table 1).

265 The cut-off rigidity values for the measurement campaigns were calculated using the
 266 PLANETOCOSMICS (<http://cosray.unibe.ch/~laurent/planetocosmics/>) toolkit for Geant4
 267 (Agostinelli et al., 2003; Allison et al., 2006; Allison et al., 2016) applying the latest version of
 268 the International Geomagnetic Reference Field (IGRF-13) (Thébault et al., 2015) for the year
 269 2019 at the corresponding coordinates during the flights and an altitude of 20 km above sea-
 270 level. It is noteworthy, that due to the shift and tilt of the dipole-like magnetic field of Earth
 271 against the rotational axis, R_C reached during the mission in Antarctica corresponded to
 272 geomagnetic shielding conditions at much lower latitudes in Europe (approximately south of
 273 Sweden or Scotland) and North America (approximately Montreal or Vancouver).

274 Primary GCR spectra have been used as described by the model by Matthiä et al. (2013)
 275 for primary GCR nuclei from hydrogen to nickel and using the Oulu NM count rates to derive
 276 the solar modulation effect and the corresponding model parameter W ($W=11.04$ for 23
 277 September 2019 and $W=11.12$ for 15 December 2019 to 16 January 2020). Dose rate profiles
 278 were calculated following the identical methodology applied earlier (Matthiä & Berger 2017;
 279 Matthiä et al., 2017; Berger et al., 2019), calculating the transport of primary GCR particles
 280 through the atmosphere with Geant4 and the resulting particle spectra at a number of different
 281 altitudes and corresponding atmospheric shielding. In a second step, the particle spectra at the
 282 different altitudes were converted to dose rates through pre-calculated fluence-to-dose
 283 conversion factors. For the one-day New Mexico flight conditions, a single set of transport
 284 calculations was produced. For the longer duration (32-day) mission in Antarctica two sets of
 285 transport calculations were performed for the extreme values of the cut-off rigidity that were
 286 reached during the mission (0 GV and 1.4 GV). The dose rates were then calculated by linear
 287 interpolation between the values at 0 GV and 1.4 GV at the respective altitudes.

288 The resulting dose rate was calculated for each particle individually and as a sum, which
 289 allowed for tracking the changing contributions through an atmospheric vertical profile. Here, we
 290 present the calculated dose rate in Si for different particles and the total dose rate in comparison
 291 to the measured dose rate.

292 4. Results

293 In the following section 4, we report results from the M-42 detector for the MARSBOx
 294 and E-MIST missions. To begin, we present the nominal count rate and dose rate data for
 295 MARSBOx (section 4.1) and E-MIST (section 4.2). Next, we compare the MARSBOx and
 296 E-MIST data at float altitudes (section 4.3), followed by a comparison of the calculated and
 297 measured count- and dose rate data in section 4.4. Finally, in section 4.5, we focus on
 298 investigations of the Regener maximum for the two mission profiles. For all absorbed dose data
 299 summarized hereafter, we refer to absorbed dose in Si.

300 4.1 MARSBOx: Measured data

301 M-42 instrument began logging data for the MARSBOx mission when powered on at
 302 14:05:33 UTC on 23 September 2019 as the balloon started its ascent to the stratosphere. Data
 303 were stored every 5 minutes up to the end of the mission (M-42 was switched off at
 304 21:15:33 UTC). Figure 3 depicts flight profile data for the entire MARSBOx mission from

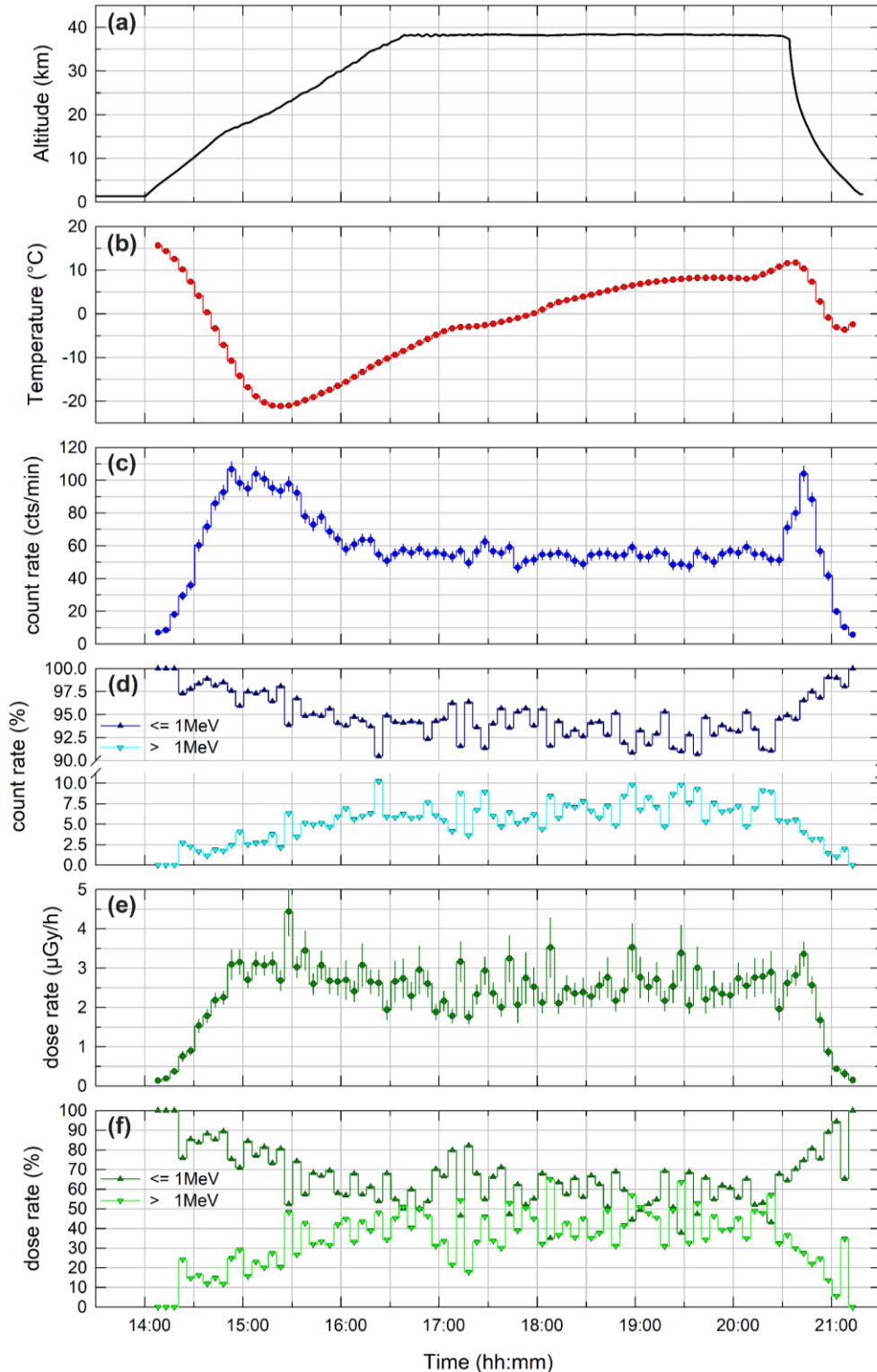
305 launch to landing. Figure 3a shows the GPS altitude of the mission (km), followed by the
 306 temperature ($^{\circ}\text{C}$) measured with the internal M-42 temperature sensor in Figure 3b. Next, Figure
 307 3c provides the measured count rate (cts/min). The measured dose rate ($\mu\text{Gy/h}$) is displayed in
 308 Figure 3e.

309 In addition, we provide data based on two distinct energy cuts for the energy deposition
 310 spectra. The M-42 system measures energy depositions (E_{Dep}) in Si from 0.07 MeV up to
 311 20 MeV. We split this energy deposition range in two intervals, the low energy deposition
 312 interval covering all $E_{Dep} \leq 1\text{MeV}$ and the high energy deposition interval covering all energy
 313 depositions $E_{Dep} > 1\text{MeV}$. The relevant percentage for the count rates and dose rates for these
 314 two E_{Dep} ranges as denoted before is provided in Figure 3d (count rates) and in Figure 3f (dose
 315 rates) of the MARSBOx mission.

316 The MARSBOx float altitude ($\sim 38\text{ km}$) was reached shortly after 16:30 UTC and the
 317 payload remained at this altitude for almost four hours. Shortly after 20:30 UTC, the balloon
 318 flight was terminated and the payload on the gondola began its parachute descent with a
 319 subsequent touch down at 21:30 UTC. Looking at the count rate data (Figure 3c), we see an
 320 increase of counts with increasing altitude, followed by a plateau around 15:00 UTC. From that
 321 point forward, the count rate decreased again until about 16:30 UTC (reaching float altitude) and
 322 stayed nearly constant to 20:30 UTC upon parachute descent. The relatively rapid descent logged
 323 an increase in count rates at around 20:45 UTC followed by a fast drop. We observe these two
 324 plateaus in the count rate as related to the crossings of the Regener maximum, i.e., slowly
 325 reached during balloon ascent and rapidly flown through during the parachute descent (see
 326 section 4.4 and 4.5 for an in-depth discussion).

327 Examining the percentage of count rates in energy bands compared to mission elapsed
 328 time (Figure 3d), we see that the low energy depositions ($E_{Dep} \leq 1\text{MeV}$) (starting with 100%
 329 close to ground) decreased to 93.5% during the float period (16:30 – 20:30 UTC) with 6.5%
 330 being the contributions from high energy depositions $E_{Dep} > 1\text{MeV}$. If we compare these values
 331 to the percentage contribution to the dose rate (Figure 3 f) for the float time of the balloon, these
 332 correspond to 59.2% for $E_{Dep} \leq 1\text{ MeV}$ and 41.8% for $E_{Dep} > 1\text{ MeV}$. In comparison, if we look
 333 at the crossings of the Regener maximum during ascent of the balloon, the percentage
 334 contribution is 97.3% to 2.8% for the count rate and 78.8% to 21.2% to the dose rate. Altogether,
 335 by comparing the Regener maximum conditions with the high-altitude float conditions, we
 336 observe an increase in high energy counts (from 2.8% to 6.5%) and the contribution from high
 337 energy depositions ($E_{Dep} > 1\text{MeV}$) to the dose rate increased from 21.2 to 41.8%. An in-depth
 338 discussion with conclusions about these results is provided later in section 4.5.

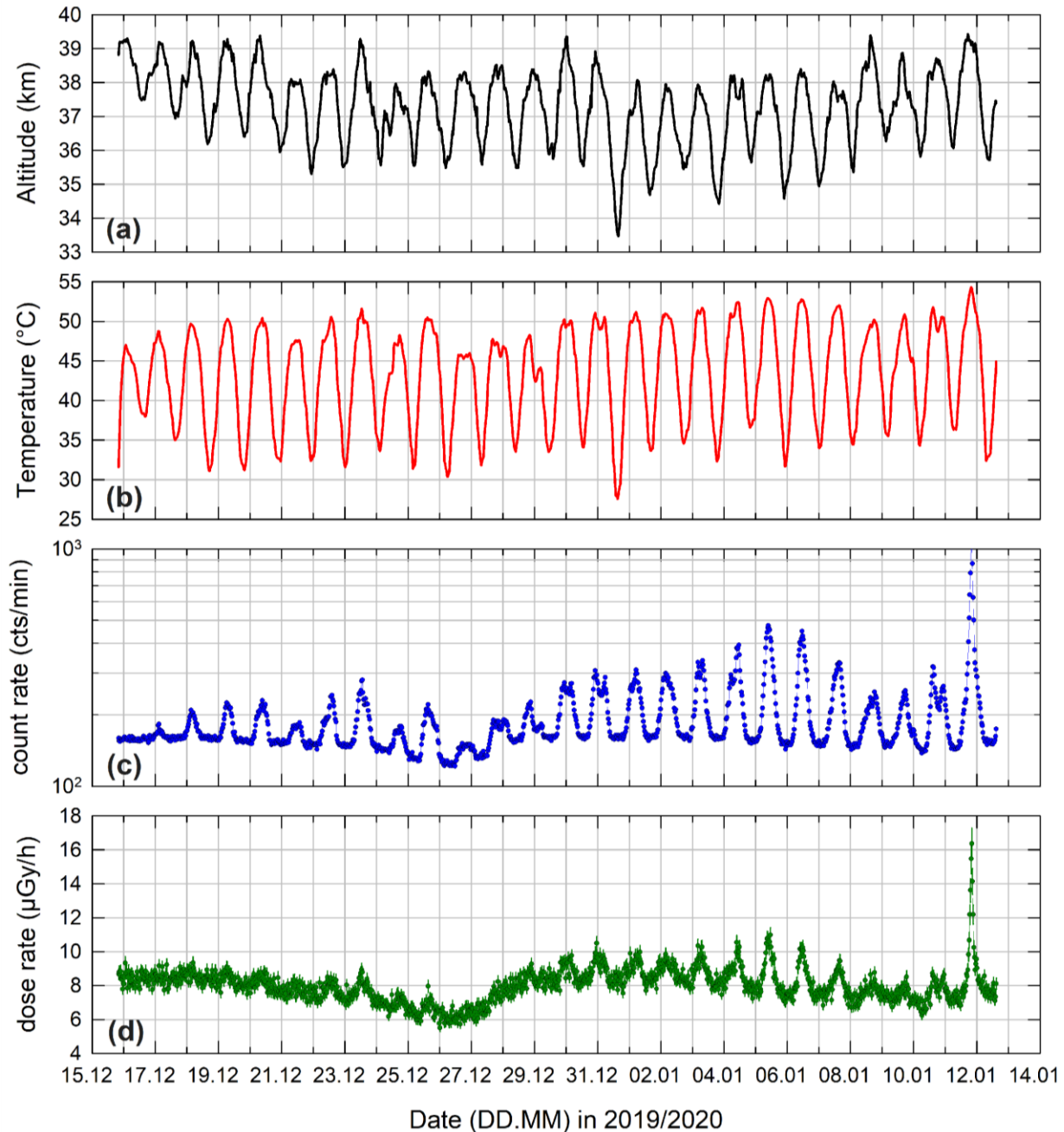
339 To summarize, the first maximum in count rates was reached at 14:53 UTC at an altitude
 340 of 17.02 km during the ascent of the balloon with a count rate of 107 ± 5 cts/min and a respective
 341 dose rate of 3.1 ± 0.4 $\mu\text{Gy/h}$. The second peak was reached at 20:43 UTC at an altitude of 17.02
 342 km during the descent of the payload with an average count rate of 104 ± 5 cts/min and a dose rate
 343 of 3.4 ± 0.3 $\mu\text{Gy/h}$. The average dose rate for the float altitude was 2.5 ± 0.4 $\mu\text{Gy/h}$ with an average
 344 count rate of 54 ± 1 cts/min. Summing up the dose contributions over the whole MARSBOx
 345 flight, we arrived at a total mission dose of 16.99 μGy .



346
 347 Figure 3. MARSBOx mission data (a) GPS altitude (km); (b) M-42 internal temperature (°C);
 348 (c) count rate (cts/min); (d) percentage of count rate for energy depositions $E_{Dep} \leq 1$ MeV and
 349 $E_{Dep} > 1$ MeV; (e) dose rate (μ Gy/h); (f) percentage of dose rate for energy depositions
 350 $E_{Dep} \leq 1$ MeV and $E_{Dep} > 1$ MeV.

351 4.2 E-MIST: Measured data

352 The M-42 detector for the E-MIST mission was powered on 15 December 2019 at
 353 13:55 UTC shortly after the balloon launched from Antarctica. The dosimeter made
 354 measurements until 12 January 2020 at 14:55 UTC, covering 28 days and 1 hour of the 32-day
 355 mission. In the following section, we present the mission profile data measured by the M-42
 356 system upon E-MIST reaching a float altitude of ~ 39 km on 15 December 2020 at 19:55 UTC.
 357 Data for the first few hours of the mission (during ascent of the balloon) will be reported later in
 358 sections 4.4 and 4.5 of this paper.



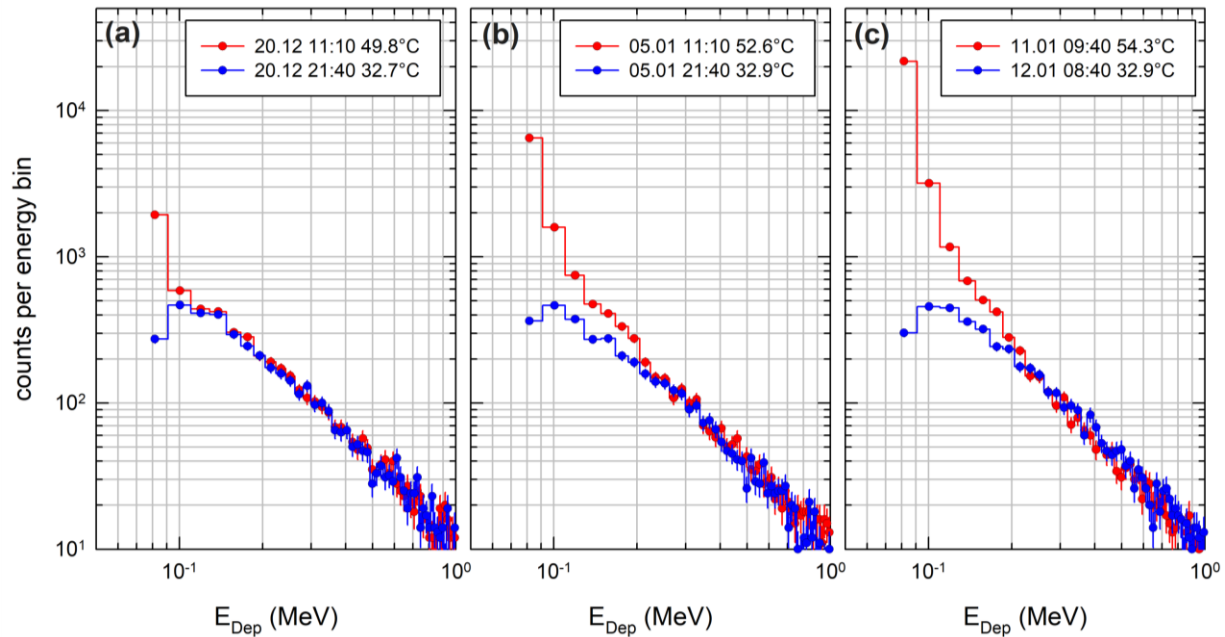
359
 360 Figure 4. E-MIST mission data (a) GPS altitude (km); (b) M-42 internal temperature ($^{\circ}$ C);
 361 (c) count rate (cts/min); (d) dose rate (μ Gy/h).

362 Figure 4a summarizes the altitude track of the E-MIST flight data, which varied about 3 km in
 363 periodic cycles due to air temperature influences during stratospheric circumnavigation. The M-
 364 42 internal temperature traced the altitude profile pattern depicted in Figure 4b; oscillation values
 365 corresponded to the flight altitude (higher altitudes had higher temperatures. M-42 measured
 366 count rate (cts/min) are shown in Figure 4c while measured dose rate ($\mu\text{Gy/h}$) is plotted in Figure
 367 4d. The count rate data also showed an oscillation, although less prominent, and lesser still for
 368 the measured dose rates. Our initial interpretation of the dataset suggested temperature
 369 influenced the M-42 count rate and, to a lesser extent, the dose rate – a topic that will be
 370 addressed next.

371 4.2.1. E-MIST: Measured data (cleaning procedures)

372 The M-42 radiation detector was designed to work at temperature environments from
 373 $-20\text{ }^\circ\text{C}$ up to $\sim +40\text{ }^\circ\text{C}$. Temperatures above $\sim 40\text{ }^\circ\text{C}$ can lead to unwanted thermal noise in the
 374 lowest energy channels of the detector, which then influences both the count- and dose rate
 375 measurements of the system. Our internal channel numbering refers to channel #22 as the lowest
 376 energy channel used for count rate and dose rate determination with an energy range from
 377 $70 - 90\text{ keV}$. Considering the possible effect of temperature during the E-MIST mission on the
 378 lower energy channels of the system (introduced in previous section 4.2), we plotted
 379 Figure 5 (a to c) to compare the energy deposition spectra measured by the M-42 system for
 380 three different dates (a) 20 December 2019, (b) 05 January 2020 and (c) 10/11 January 2020;
 381 each date included two distinct temperature cases: the first case (*cold case*) shows the energy
 382 deposition spectra for measured temperature values between 32.7 and $32.9\text{ }^\circ\text{C}$ whereas the
 383 second case (*hot case*) shows the energy spectra for measured temperature values of $49.8\text{ }^\circ\text{C}$ (20
 384 December 2019), $52.6\text{ }^\circ\text{C}$ (05 January 2020) and $54.3\text{ }^\circ\text{C}$ (the highest temperature reached during
 385 the flight on 11 January 2020).

386



387 Figure 5. Comparison of *cold* and *hot* energy deposition spectra for three dates within the
 388 E-MIST mission: (a) 20 December 2019; (b) 05 January 2020 and (c) 11/12 January 2020.
 389 Note: For a better comparison the energy deposition range is limited to $E_{Dep} \leq 1\text{ MeV}$.
 390

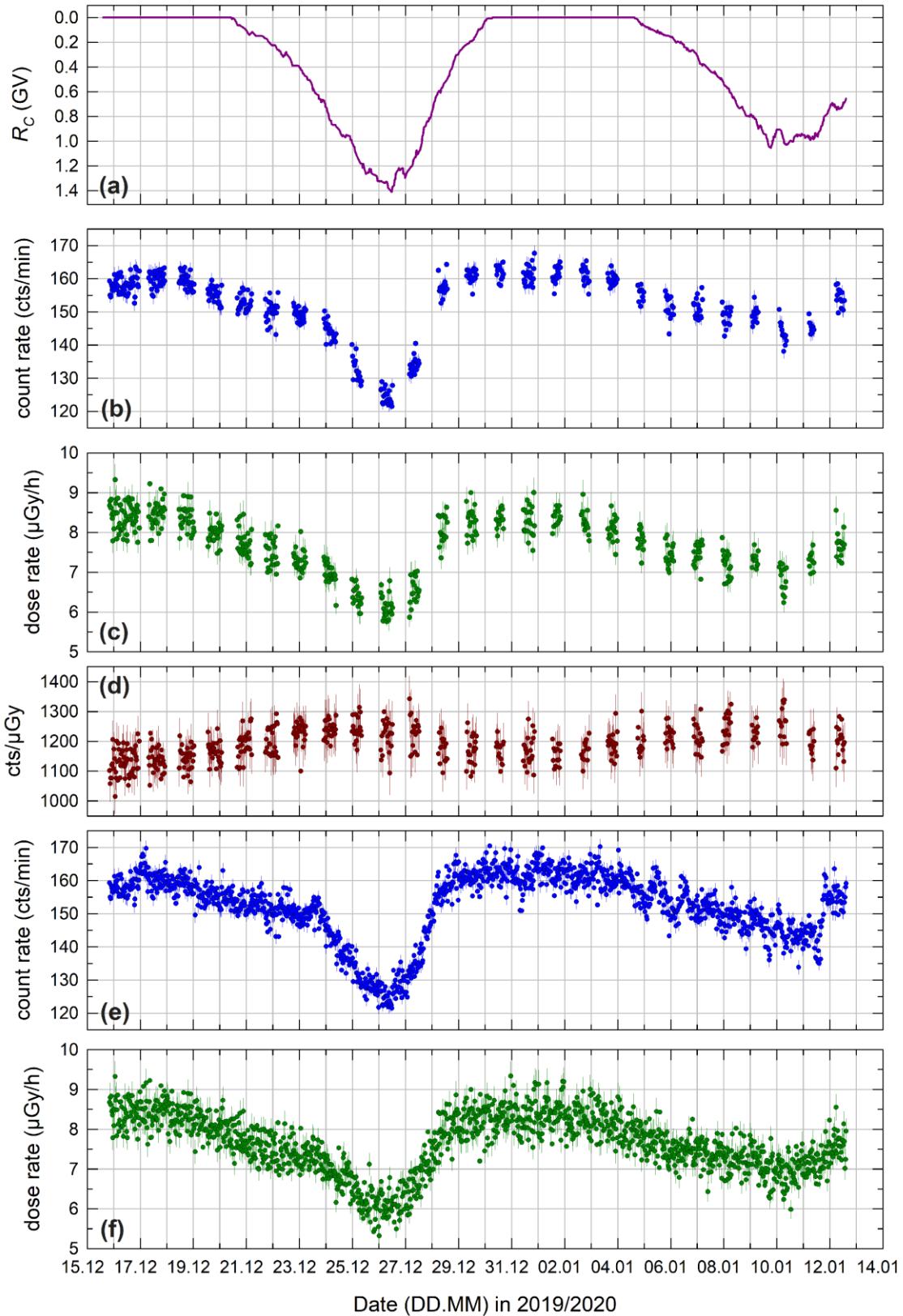
391 When comparing the spectra, one clear pattern is the increase of counts in the lower
 392 energy bins of the data (up to ~ 180 keV, which equals channel #27 of the spectra) over the
 393 duration of the mission (i.e., chronologically depicted across Figure 5a to Figure 5c). From ~ 180
 394 keV onwards, there was no difference between the two spectra and the relevant dose values for
 395 all three comparisons. As example the dose value from channel #27 onwards for the
 396 10/11 January 2020 are 6.43 ± 0.44 μGy for the *hot* case and 6.44 ± 0.46 μGy for the *cold* case.
 397 This indicated a need to “*clean*” the data due to effect of increasing temperature on the
 398 instrument sensitivity. One straightforward procedure would be to only trust data acquired at
 399 temperature values $\leq 40^\circ\text{C}$, following the M-42 system operating requirements. But such an
 400 approach would fail to consider how the oscillation of the count rate increased over the course of
 401 the E-MIST mission time (that might be related to an overall temperature creep of the system).

402 Therefore, a different approach was taken to deal with the thermal uncertainties on
 403 system performance, following a two-step progression. The first step limited the data based on
 404 the measured count rate in the lowest used M-42 energy channels. If the count rate in channel
 405 #22

406 (70 – 90 keV) was lower than the count rate in channel #23 (90 – 110 keV), the data were
 407 considered *clean*. We define *clean* as data not influenced by increasing temperatures. Following
 408 this procedure, the total amount of E-MIST mission data on the M-42 was reduced to 262 hours,
 409 averaging ~ 9 hours of data per day. Because the energy depositions and subsequent dose values
 410 above ~ 180 keV were not influenced by the temperature, we were aiming to impose a second
 411 check on the raw data. The second step had the following logic: If we assume, that from channel
 412 #27 onwards, or values of ~ 180 keV (see spectra in Figure 5), there was no temperature
 413 influence on the energy deposition spectra, we could use the *clean* data set to generate ratios
 414 between count- and dose rates from channel #22 onwards versus count- and dose rates from
 415 channel #27 onwards. Then those ratios could be used (based on interpolation) to re-scale the
 416 channel #27 count- and dose rate data for the hot temperature cases. This cleaning approach
 417 created an additional *interpolated* dataset for the times where the temperature was too high (and
 418 M-42 data in the lowest energy channels could not be trusted), and filling in the gaps for a full,
 419 cleaned set of mission measurements.

420 4.2.2. E-MIST: Measured data (*clean + interpolated*)

421 Based on the information and analysis presented in the previous section 4.2.1., we can
 422 now provide the *clean* and the *clean + interpolated* M-42 dataset for the E-MIST mission in
 423 Figure 6. We show in Figure 6a the calculated cut-off rigidity (R_C) over the mission. The *clean*
 424 dataset is in Figure 6b and Figure 6c. With Figure 6d, we provide the ratio between counts and
 425 dose (cts/ μGy). The ratio changed over the mission, dependent on R_C . The lower the R_C , the
 426 lower the cts/ μGy ratio. This indicated that by flying to higher R_C values, the energy deposition
 427 spectra changed, and thus, more counts were needed to reach 1 μGy of dose (compared to lower
 428 R_C values). Finally, Figure 6e and Figure 6f then show the *clean + interpolated* count- and dose
 429 rate profile over the float times for the E-MIST mission. Notably, this dataset represents almost
 430 two full circumnavigations of the Antarctic continent by the balloon carrying the payload. The
 431 count- and dose rate follow the expected R_C values, reaching the lowest points at 26 December
 432 2019, then climbing again and reaching a second minima on 10 January 2021. The second
 433 minimum was not as pronounced, due to the fact that the balloon did not reach the same R_C
 434 values as it did for the first minimum (R_C close to 1.4 GV on 26 December 2019; R_C close to 1.0
 435 GV at 11 January 2020).

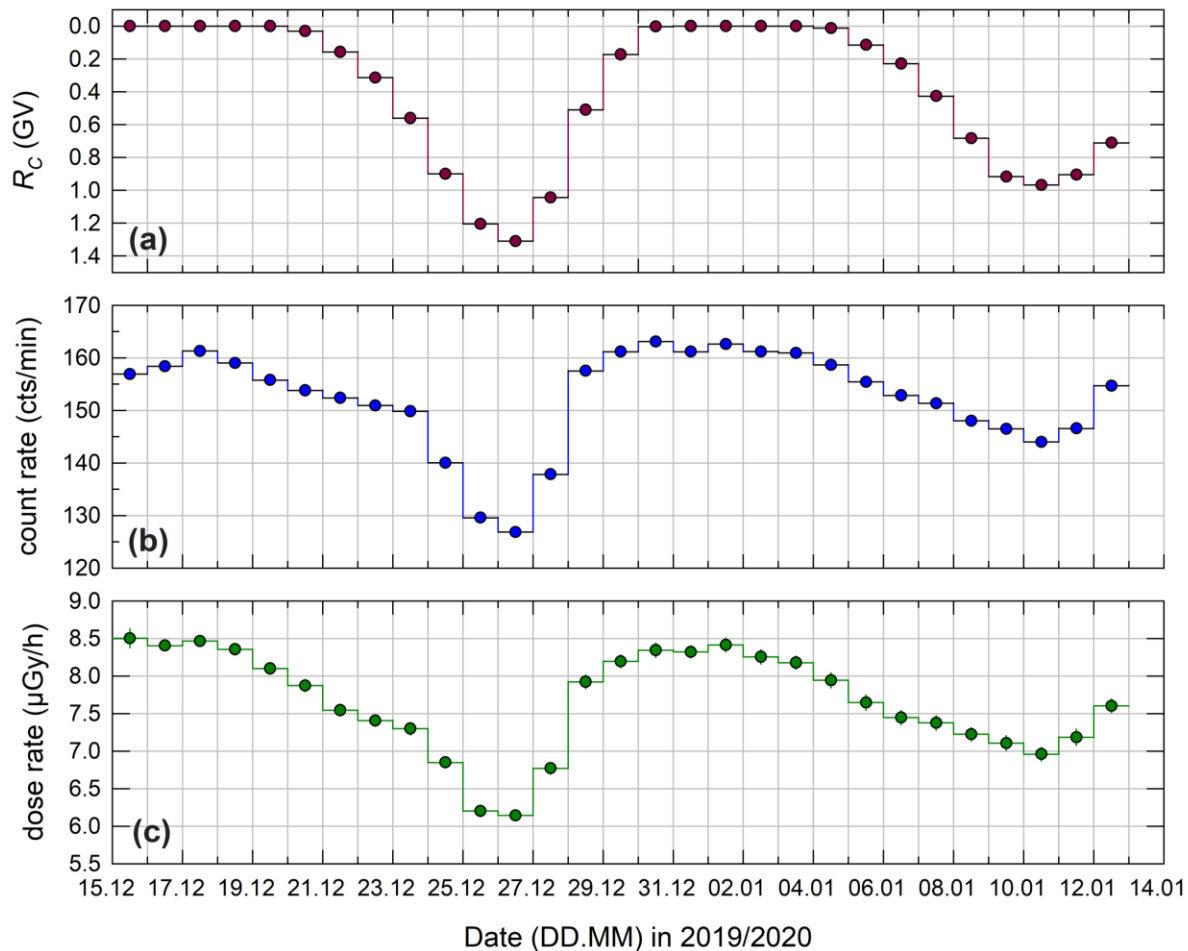


436
437
438

Figure 6. E-MIST mission data (a) cut-off rigidity, or R_C ; (b) count rate (*clean*); (c) dose rate (*clean*); (d) cts/ μGy ; (e) count rate (*clean + interpolated*); (f) dose rate (*clean + interpolated*)

439 (see also Figure A4, A5 and A6 for the data of the R_C , the count rate (*clean + interpolated*) and
 440 the dose rate (*clean + interpolated*) over the flown mission trajectory).
 441

442 To better visualize the data, we show in Figure 7a, the average daily R_C and the average
 443 daily count- and dose rate values in Figure 7b and Figure 7c, respectively. The count rate pattern
 444 mirrored the dose rate pattern, as expected for the related measurements. The total mission dose
 445 at float altitude for the 28-day measurement period accounted for 5.1 mGy with a spread in daily
 446 dose values of 8.5 $\mu\text{Gy}/\text{day}$ on 17 December 2019, dropping down to 6.1 $\mu\text{Gy}/\text{day}$ on 26
 447 December 2019, then reaching maximum values of 8.4 $\mu\text{Gy}/\text{day}$ on 1 January 2020, before the
 448 next minimum of 6.9 $\mu\text{Gy}/\text{day}$ on 10 January 2020.
 449



450
 451

452 Figure 7. Daily dose values for E-MIST, depicting (a) cut-off rigidity, or R_C ; (b) count rate
 453 (cts/min); (c) dose rate ($\mu\text{Gy}/\text{h}$).

454 4.3 MARSBOx & E-MIST: Comparison at float altitudes

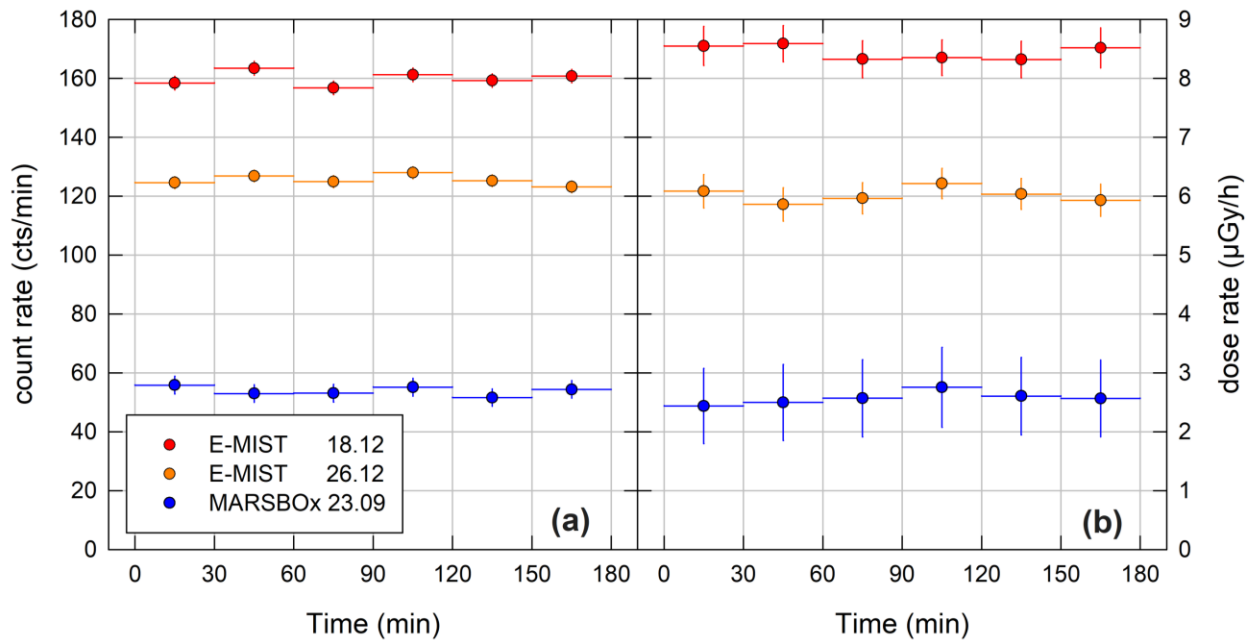
455 The following data are based on three hours of measurements for both experiments in
 456 order to make direct comparisons of the stratosphere radiation environment for polar and mid-
 457 latitude locations. Representative data from MARSBOx over New Mexico were taken for three
 458 hours at float altitude on 23 September 2019 from 17:00 – 20:00 UTC. Data from E-MIST over

459 Antarctica were taken for three hours at float on two different days: 18 December 2019 15:25 –
 460 18:25 UTC and also 26 December 2019 from 03:55 – 06:55 UTC. Two, three-hour E-MIST
 461 datasets were chosen based on the fact that on 18 December 2019 the balloon flew at $R_C = 0$ GV
 462 and at 26 December 2019 it reached a R_C of 1.33 GV. All relevant data for this comparison of
 463 MARSBOx and E-MIST measurements are summarized in Table 2 and the measured count- and
 464 dose rate profiles are shown in Figure 8.

465
466 Table 2467 *Count rates and dose rates for three 3-hour time periods for MARSBOx and E-MIST*

Mission	Date	Time	Mean altitude (km)	R_C (GV)	Count rate (cts/min)	Dose rate (μ Gy/h)	cts/ μ Gy
E-MIST	18. Dec. 2019	15:25 – 18:25	36.3	0	160 \pm 2	8.4 \pm 0.3	1136
	26. Dec. 2019	03:55 – 06:55	35.7	1.33	125 \pm 2	6.0 \pm 0.3	1251
MARSBOx	23 Sept. 2019	17:00 – 20:00	38.3	3.95	54 \pm 1	2.5 \pm 0.4	1256

468



469

470

471 Figure 8. Comparing MARSBOx (23 September 2019) and E-MIST (18 and 26 December 2019)
 472 missions over representative, three-hour time intervals with (a) count rate (b) dose rate.

473

474

475

476

477

478

479

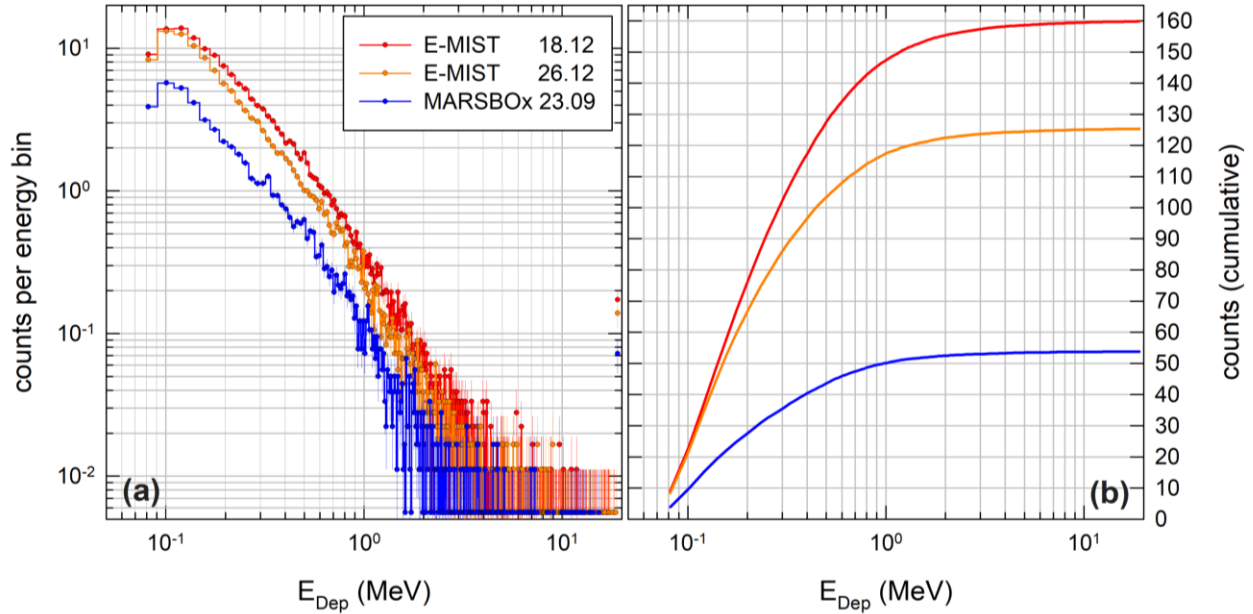
480

481

482

With the E-MIST snapshot, the clear dependence of count- and dose rate on R_C can be noted. The ratio of cts/ μ Gy (i.e., counts needed to reach 1 μ Gy of dose) also increased with R_C , which can be explained by a softening of the energy deposition spectra going to higher cut-off rigidities. Furthermore, by examining the energy deposition spectra for the same 3-hour periods, the effect of the geomagnetic cutoff on the spectra stands out. For instance, in Figure 9a, we depict the spectra for each mission (as summarized in Table 2) with the limitation to E_{Dep} in Si ≤ 1 MeV. The three spectra clearly differed in dependence on R_C . Next, with Figure 9b, we illustrate the cumulative counts for the three distinct positions over New Mexico and Antarctica – again, this clearly demonstrated the energy deposition spectral reliance on changes in R_C (from

483 0 GV at 18 December and 1.33 GV at 26 December 2019 for E-MIST and to 3.95 GV for
 484 MARSBOx on 23 September 2019).



485
 486

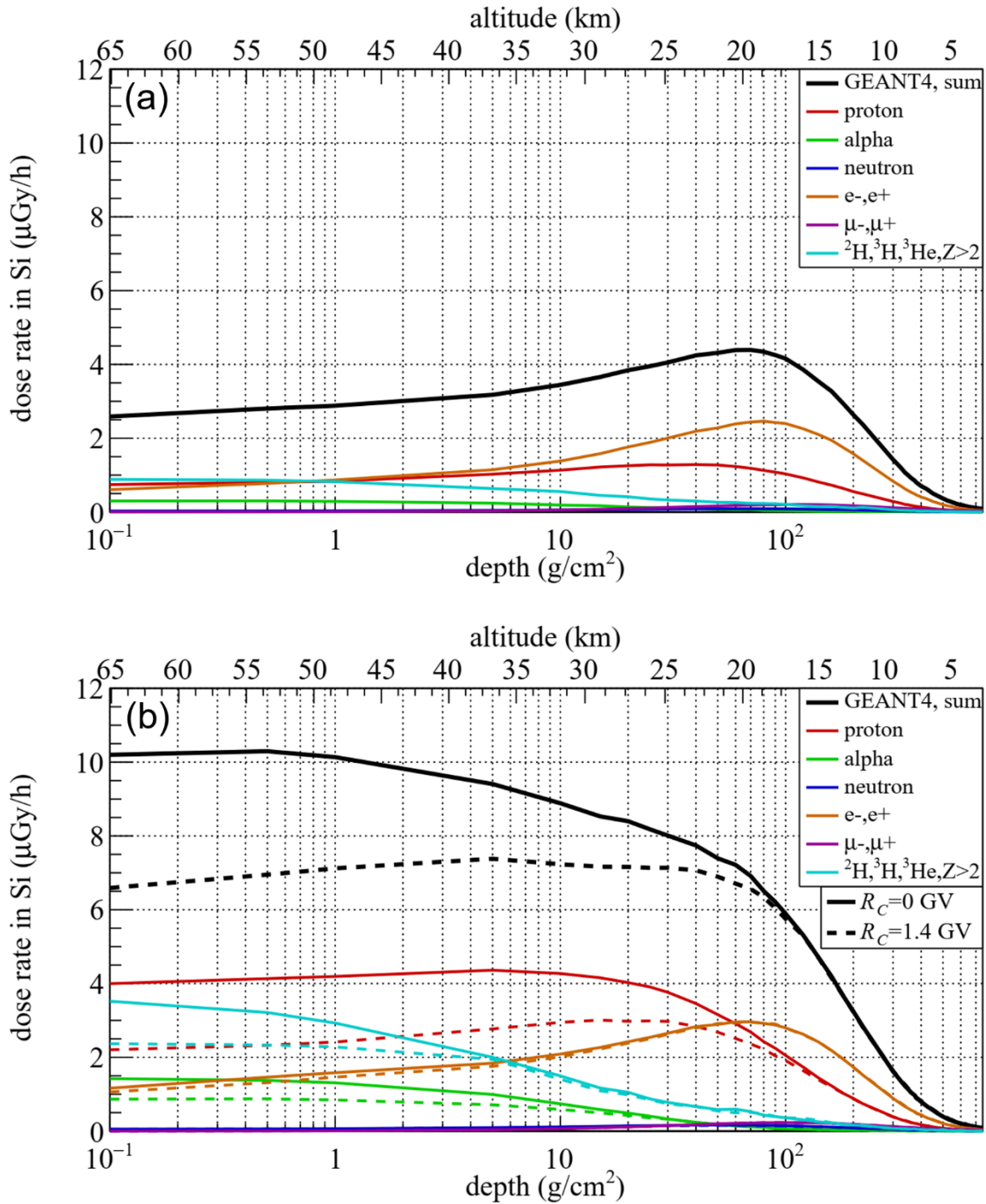
487 Figure 9. (a) Energy deposition spectra collected over a 3 hr period at float altitude for
 488 MARSBOx (23 September 2019, $R_C = 3.95$ GV) and for E-MIST (18 December 2019, $R_C = 0$
 489 GV; 26 December 2019, $R_C = 1.33$ GV); (b) cumulative counts for MARSBOx and E-MIST.

490 4.4 MARSBOx & E-MIST: Comparing model and measurement results

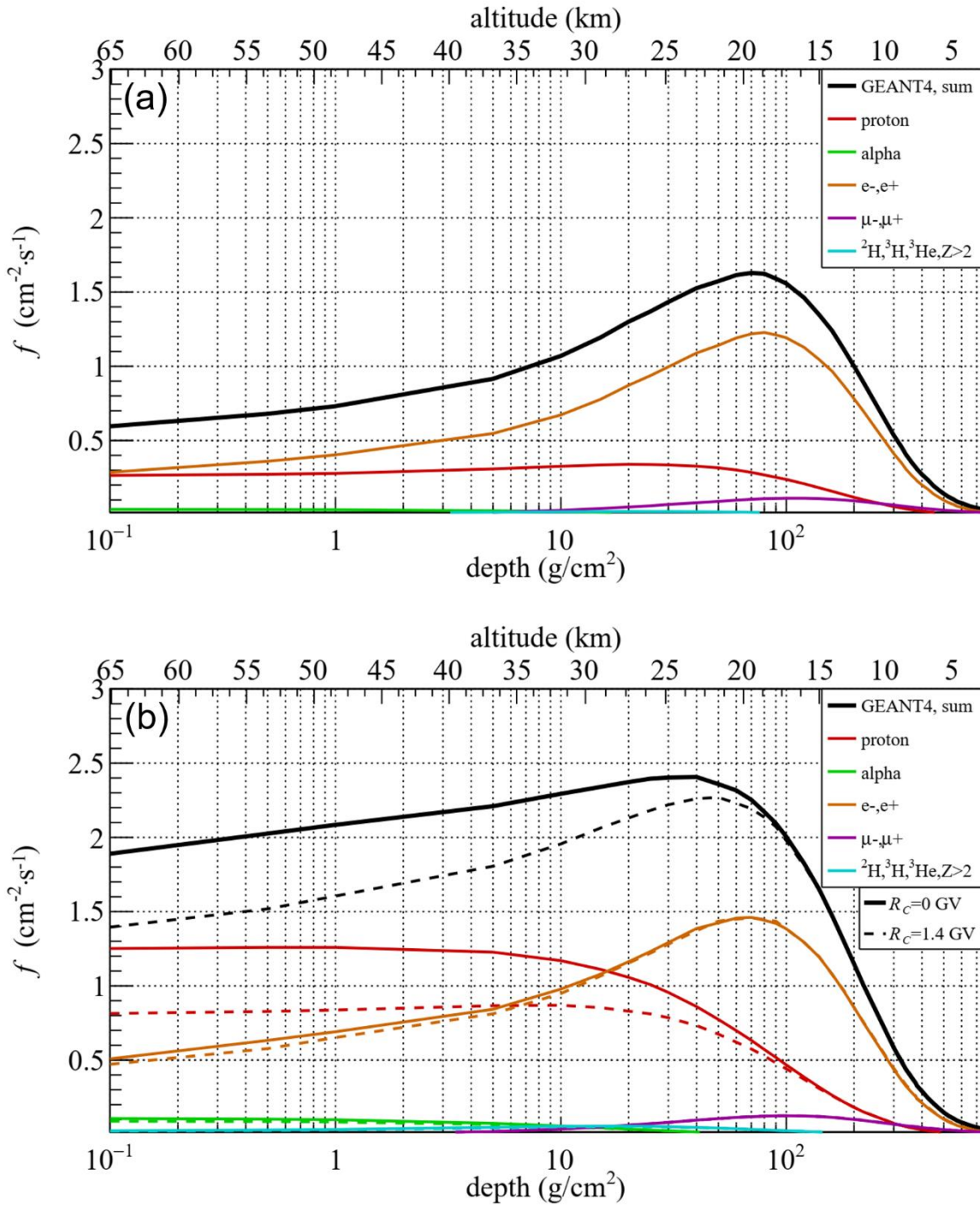
491 Within this section 4.4 we will compare model results with the measurements for
 492 MARSBOx and E-MIST. First, we will present the calculated dose rate and planar fluence rate
 493 for the MARSBOx and E-MIST flights in section 4.4.1. This will be followed by analysis of the
 494 correction factors (cf) to be applied for the calculated data in order to cope with the energy
 495 deposition range (E_{Dep}) of the M-42 system in section 4.4.2. Section 4.4.3 will then present the
 496 final comparison of calculated and measured data.

497 4.4.1. Calculated dose and fluence rates

498 Geant4 modeling results for dose rate and planar fluence rate of charged particles are
 499 shown in Figure 10 and Figure 11, respectively. In each figure, Panel a displays the results for
 500 the prevailing conditions during the MARSBOx flight and Panel b for the E-MIST flights. The
 501 planar fluence rate represents the number of particles traversing a given plane per area and time,
 502 measurable from the recorded count rate of a planar detector divided by its area (e.g., for the
 503 M-42 a count rate divided by 1.22 cm²). For an isotropic field, the particle fluence is two times
 504 the planar particle fluence. The solid and dashed lines in the lower panels of Figure 10 and
 505 Figure 11 show results for the extreme values of the geomagnetic shielding that were reached
 506 during the E-MIST mission (solid lines: $R_C = 0$ GV; dashed lines: $R_C = 1.4$ GV). Figure 10 shows
 507 the calculated dose rate profile dependent on the atmospheric shielding (altitude) for the different
 508 geomagnetic shielding conditions in New Mexico (Figure 10 a) compared to the more extreme
 509 values in Antarctica (Figure 10 b).



510
 511
 512 Figure 10. The dose rate in Si as calculated for (a) MARSBOx ($R_C = 3.95$ GV) over New Mexico
 513 and (b) E-MIST ($R_C = 0$ GV and $R_C = 1.4$ GV) over Antarctica.
 514
 515
 516
 517



518 Figure 11. The planar fluence rate of charged particles for (a) MARSBOx ($R_C = 3.95$ GV) over
 519 New Mexico and (b) E-MIST ($R_C = 0$ GV and $R_C = 1.4$ GV) over Antarctica.
 520
 521

522 Our model results predicted dissimilar dose rate profiles for the different conditions: a
 523 pronounced maximum in dose rate at around 60 g/cm^2 to 80 g/cm^2 (20 km to 18 km) for the
 524 highest geomagnetic shielding at $R_C = 3.95$ GV in New Mexico, a plateau-like profile reaching
 525 approximately constant values above 40 g/cm^2 (≈ 22 km) for $R_C = 1.4$ GV, and a dose rate almost

526 monotonically increasing towards space reaching maximum values at an atmospheric shielding
 527 below 1 g/cm^2 ($>50 \text{ km}$) for zero geomagnetic shielding over Antarctica. The differing dose rate
 528 profiles can be explained by the composition of the radiation field (i.e., the dose rate in Si at
 529 higher cut-off rigidities is increasingly dominated by the secondary electron field).

530 The electron field is much less affected by the geomagnetic shielding and due to the fact,
 531 that the electrons are secondary particles created in the atmosphere (electrons contribute only a
 532 few percent to the primary cosmic radiation and are neglected in the model), the field has a
 533 pronounced maximum between $15 - 20 \text{ km}$ (shown in Figure 11). Protons and heavier nuclei, on
 534 the other hand, do not show such a clear maximum, neither in dose rate nor in fluence rate. At
 535 low geomagnetic shielding, the large relative contribution of protons and heavier nuclei to the
 536 dose rate (that additionally increases with altitude), compensated for the decrease in the dose rate
 537 from secondary electrons preventing the formation of a maximum (also visible in our Antarctic
 538 dataset for E-MIST, see below). For charged particle fluence rate, the situation is slightly
 539 different. Although the contribution of protons to the total fluence rate is much greater at low
 540 geomagnetic shielding and monotonically increase towards higher altitudes, it cannot quite
 541 compensate for the decrease in secondary particle fluence rate. Consequently, and consistent
 542 with our experimental data (discussed below), the charged particle fluence rate forms a
 543 maximum even at low geomagnetic shielding, but it is less pronounced and at higher altitudes
 544 ($20 \text{ km} - 25 \text{ km}$) compared to higher geomagnetic shielding ($15 \text{ km} - 20 \text{ km}$).

545 4.4.2. Correcting for the sensitivity range of the M-42 detector

546 When comparing the Geant4 model to the experimental results, the measurement range of
 547 the M-42 instrument (0.07 to 20 MeV) must be considered. The limitation to energy depositions
 548 above 0.07 MeV and below 20 MeV in the detector meant that a certain fraction of the linear
 549 energy transfer (LET) spectrum could not be measured (e.g., for particles perpendicular to the
 550 detector the cutoff would be for particles below $0.07 \text{ MeV}/0.3 \text{ mm} \approx 0.23 \text{ keV}/\mu\text{m}$ and above
 551 $20 \text{ MeV}/0.3 \text{ mm} \approx 66.7 \text{ keV}/\mu\text{m}$). The fraction of dose that was not measured depended on the
 552 contribution of low- and high-LET particles below and above the thresholds to the total dose.
 553 Using numerical simulations of the distribution of energy depositions in the planar detector, the
 554 fraction of dose caused by particles within the sensitivity thresholds of the detector was estimated
 555 to be between 0.85 and 0.96 for atmospheric shielding of 5 g/cm^2 ($\approx 36 \text{ km}$), 200 g/cm^2 ($\approx 12 \text{ km}$)
 556 and 1000 g/cm^2 ($\approx 0.3 \text{ km}$), as summarized in Table 3. The fraction was lowest (≈ 0.87) for high
 557 altitudes with an atmospheric shielding of 5 g/cm^2 and it increased toward lower altitudes (≈ 0.94
 558 at 200 g/cm^2) and grew further near the ground (i.e., during balloon ascent and descent). The
 559 lowest shielding approximately corresponded to the maximum altitude that was reached during
 560 the balloon flights. The fraction of dose that was measured by the detector also showed a weak R_C
 561 dependence and decreased slightly for the geomagnetic shielding corresponding to the mission in
 562 New Mexico ($R_C \approx 3.95$); an identical trend with higher fractions occurred toward lower altitudes.
 563 This trend can be explained by the increasing contribution of high-LET particles, primary GCR
 564 nuclei, at high altitudes (thus, low mass shielding), which were above the sensitivity range of the
 565 detector. More specifically, an increasing fraction of nuclei undergo fragmentation and would be
 566 stopped before reaching lower altitudes, leading to a smaller fraction of high-LET particles. The
 567 second trend (also summarized in Table 3) was the increase of the contribution to dose from
 568 particles below the sensitivity range of the detector, caused by the formation of the secondary
 569 low-LET electron field. This increase, however, was weaker than the decrease in the high-LET
 570 particle above the sensitivity range.

571 Table 3

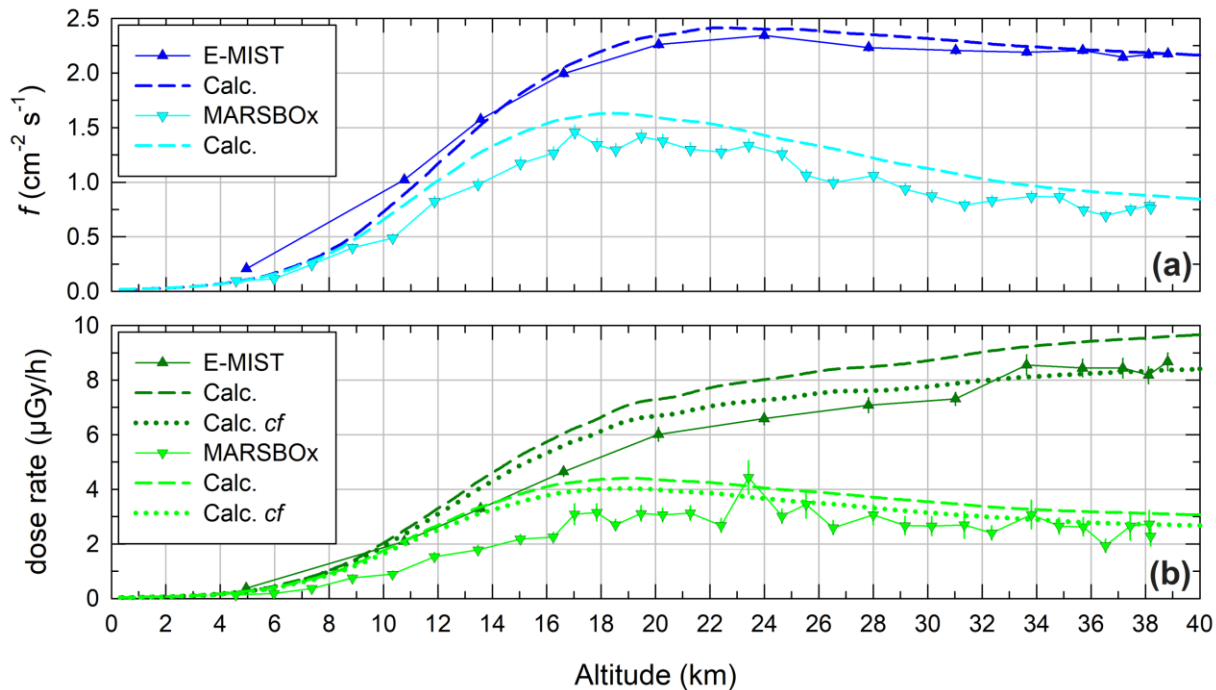
572 *Calculated fraction of dose for energy depositions E_{Dep} below ($E_{Dep} < 0.07$ MeV), above (E_{Dep}*
 573 *>20 MeV) and for the sensitivity range (0.07 MeV $\leq E_{Dep} \leq 20$ MeV) covered by the detector.*
 574 *The correction factors cf applied to the modeled dose rates for the direct comparison to the*
 575 *measurements were the factors for energy depositions within the sensitivity range of the detector.*
 576 *The atmospheric depth d is the mass shielding equivalent derived from the pressure in the*
 577 *standard atmosphere at the corresponding altitude. Relevant data is provided for E-MIST at*
 578 *$R_C=0$ GV and $R_C=1.4$ GV and for MARSBOx at $R_C= 3.95$ GV.*

Mission	E_{Dep} (MeV)	R_C (GV)	d (g/cm ²)	altitude (km)	Dose (% of total)	cf
E-MIST	<0.07	0	5	35.91	1.1	0.876
	>20				11.4	
	≥ 0.07 and ≤ 20				87.6	
	<0.07	0	200	11.91	4.3	0.939
	>20				1.8	
	≥ 0.07 and ≤ 20				93.9	
	<0.07	0	1000	0.275	3.5	0.962
	>20				0.3	
	≥ 0.07 and ≤ 20				96.2	
	<0.07	1.4	5	35.91	1.4	0.854
	>20				13.2	
	≥ 0.07 and ≤ 20				85.4	
MARSBOx	<0.07	3.95	5	35.91	2.1	0.871
	>20				10.8	
	≥ 0.07 and ≤ 20				87.1	
	<0.07	3.95	200	11.91	4.7	0.936
	>20				1.7	
	≥ 0.07 and ≤ 20				93.6	
	<0.07	3.95	1000	0.275	3.8	0.956
	>20				0.6	
	≥ 0.07 and ≤ 20				95.6	

579 4.4.3. E-MIST & MARSBOx: calculated and measured data

580 Planar fluence rates and dose rates versus altitude measured during the ascents of the
 581 E-MIST and MARSBOx missions were compared to model data in Figure 12a and Figure 12b,
 582 respectively. Measurements are given by solid lines with symbols and model results as dashed
 583 lines. Additionally, for the dose rate, the model data were multiplied by the calculated correction
 584 factor (cf) (dotted lines) for the sensitivity range of the detector (see Table 3) to facilitate a direct
 585 comparison to experimental data. In general, the agreement between model and experimental
 586 data was strong, with a slight overestimation for the MARSBOx flight, especially for the dose
 587 rate at altitudes below 20 km. While the source of this overestimation was unclear, we consider it

588 a high-priority target for future investigation. Possible explanations include the production of
 589 secondary particles that could be overestimated by the model, or that the geomagnetic shielding
 590 was not perfectly reproduced by the effective vertical cut-off rigidity that was used in this work.



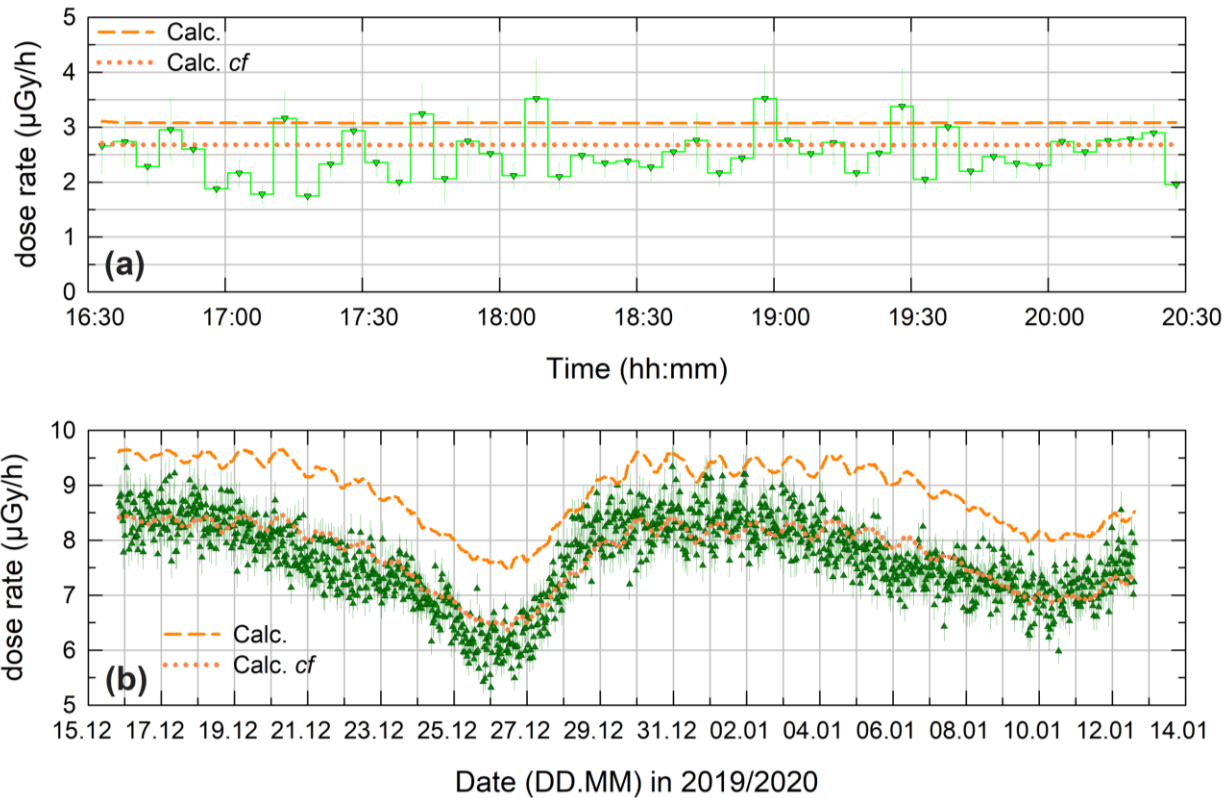
591
 592
 593
 594
 595

Figure 12. During E-MIST and MARSBOx balloon ascent, comparing measured and calculated (a) planar fluence rates and (b) dose rates. cf = correction factor (see text).

596 One takeaway from Figure 12a was confirming the model prediction of a maximum in the
 597 fluence rate at around 15 – 20 km at higher geomagnetic shielding (New Mexico,
 598 $R_C = 3.95$ GV) and with less significance the maximum at around 20 – 25 km at low geomagnetic
 599 shielding (Antarctica, $R_C = 0$ GV). Due to the statistical variations in the experimental data,
 600 however, it was difficult to identify a maximum in the dose rate (Figure 12b), but it seems
 601 plausible. On the other hand, it was clear that no such dose rate maximum exists for low
 602 geomagnetic shielding. Also related to this phenomenon is the solar modulation, which likely
 603 plays a role in the question if a maximum in dose rate forms in the atmosphere. As introduced
 604 earlier, our missions were flown during very weak solar activity and very high GCR intensity.
 605 Higher solar activity would suppress the intensity of lower energetic primary particles, leading to
 606 the formation of a maximum similar and synergetic to higher geomagnetic shielding. A valuable
 607 topic for future research would be to explore the extent to which a stronger solar modulation
 608 leads to a clear maximum in dose rate at low geomagnetic shielding, and also how high cut-off
 609 rigidities would affect the overall dose rate profile. Herein, our model calculations suggest that
 610 for solar maximum conditions, no clear maximum would form in the dose rate profile at zero
 611 geomagnetic shielding, but that the curve would flatten and form a plateau similar to the low
 612 geomagnetic shielding (Figure 10b, $R_C = 1.4$ GV) and solar minimum conditions.

613 Another aspect of Figure 12b worth emphasizing is the correction factor (cf) for the
 614 sensitivity range of the M-42 detector, which can explain most of the discrepancies between the
 615 calculated dose rate and measurements (except for the overestimation of the dose rates measured

616 during the MARSBOx campaign at altitudes <20 km). Our correction factors were linearly
 617 interpolated for altitudes between the values given in Table 3 for each corresponding mission.
 618



619
 620
 621 Figure 13. (a) MARSBOx – comparison of measured (green) and calculated (orange dashed
 622 lines) and corrected calculated (orange dotted line) dose rate for the time at float altitude;
 623 (b) E-MIST – comparison of measured (green) and calculated (orange dashed lines) and
 624 corrected calculated (orange dotted line) dose rate for the time at float altitude (see also Figure
 625 A7 and A8 for the calculated dose rate (with cf) and the calculated dose rate over the mission
 626 trajectory).

627
 628 With Figure 13, we show measured and calculated dose rates at float altitude for the
 629 MARSBOx and E-MIST flights over mission time. Our model calculated total dose rates (dashed
 630 lines) were multiplied by the M-42 detector sensitivity factor (correction factor cf) from Table 3
 631 (dotted line). For the MARSBOx data, a constant factor of 0.871 was applied, corresponding to a
 632 cut-off rigidity $R_C = 3.95$ GV and an altitude of 35.9 km. For the E-MIST data, the corresponding
 633 correction factor was calculated from a linear interpolation in the cut-off rigidity along the flight
 634 trajectory between the two extreme values at 35.9 km given in Table 3: 0.876 at $R_C = 0$ GV and
 635 0.854 at $R_C = 1.4$ GV. From the model, total dose rates for E-MIST were calculated for the
 636 boundary conditions of the two, 3-hour intervals in Table 2 and were $9.3 \mu\text{Gy/h}$ ($R_C = 0$ GV) and
 637 $7.6 \mu\text{Gy/h}$ ($R_C = 1.33$ GV); these values reduced to $8.2 \mu\text{Gy/h}$ and $6.5 \mu\text{Gy/h}$, respectively, when
 638 the corresponding correction factors were applied. The detector sensitivity corrected model
 639 values were compatible with the measured data: $8.4 \pm 0.3 \mu\text{Gy/h}$ ($R_C = 0$ GV) and $6.0 \pm 0.3 \mu\text{Gy/h}$
 640 ($R_C = 1.33$ GV). The corresponding values for the 3-hour interval from the MARSBOx mission

641 at $R_C = 3.95$ GV were $3.1 \mu\text{Gy/h}$ (total calculated), $2.7 \mu\text{Gy/h}$ (calculated times correction factor)
 642 and $2.5 \pm 0.3 \mu\text{Gy/h}$ (measured).

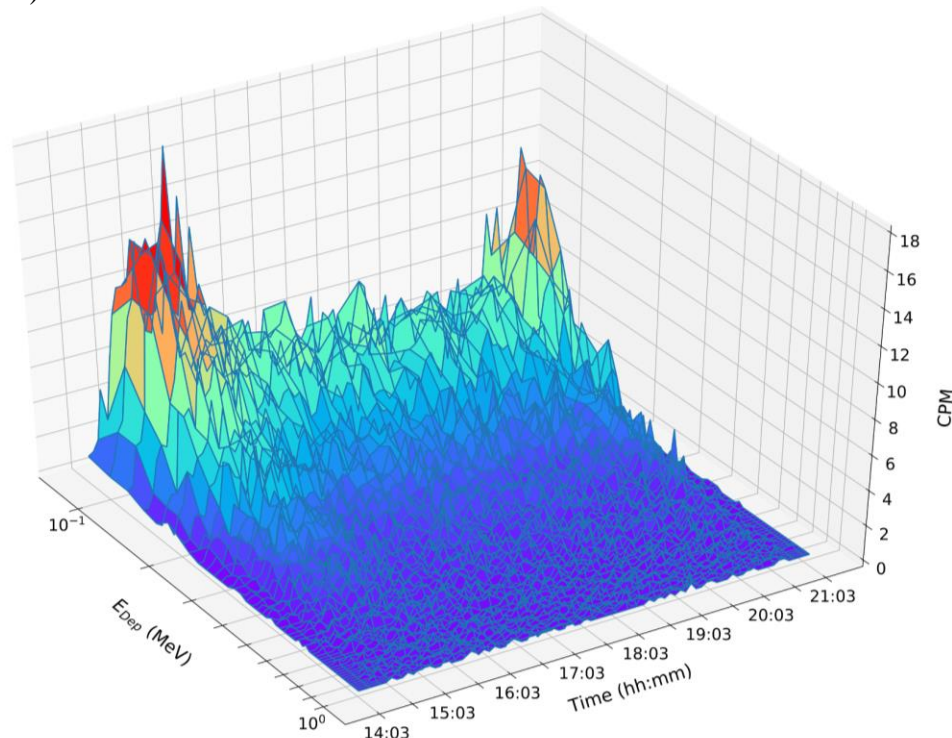
643 Interestingly, Figure 13 also demonstrated how the overestimation of the model data
 644 could be consistently explained by the limited measurement range of the detector. For instance,
 645 variations of the dose rates caused by changing geomagnetic shielding along the E-MIST flight
 646 path were nicely reproduced by the model when applying the effective vertical cut-off rigidity to
 647 the primary GCR spectra. In addition, measurements performed by the DLR Eu:CROPIS
 648 RAMIS (Hauslage et al., 2018) detector (at approximately 600 km altitude in a polar orbit at the
 649 time of the E-MIST flight) also indicated that the additional dose in Si from energy depositions
 650 between 20 MeV and 200 MeV accounted for $\sim 12\%$ of the total dose in the south polar region.

651 4.5 MARSBOx & E-MIST: The Regener Maximum

652 After summarizing measured and modeled radiation results, we now transition to data
 653 analysis for crossings of the Regener maxima during each balloon flight mission, starting with
 654 MARSBOx (section 4.5.1) and followed by E-MIST (section 4.5.2).

655 4.5.1. MARSBOx – ascent and descent

656 The count- and dose rate data provided in Figure 3 show two crossings of the Regener
 657 maximum; one during the slow ascent of the balloon system over New Mexico and the other
 658 during the fast descent of the payload (on parachute after mission termination the descent rate
 659 was ~ 1.4 km/min).

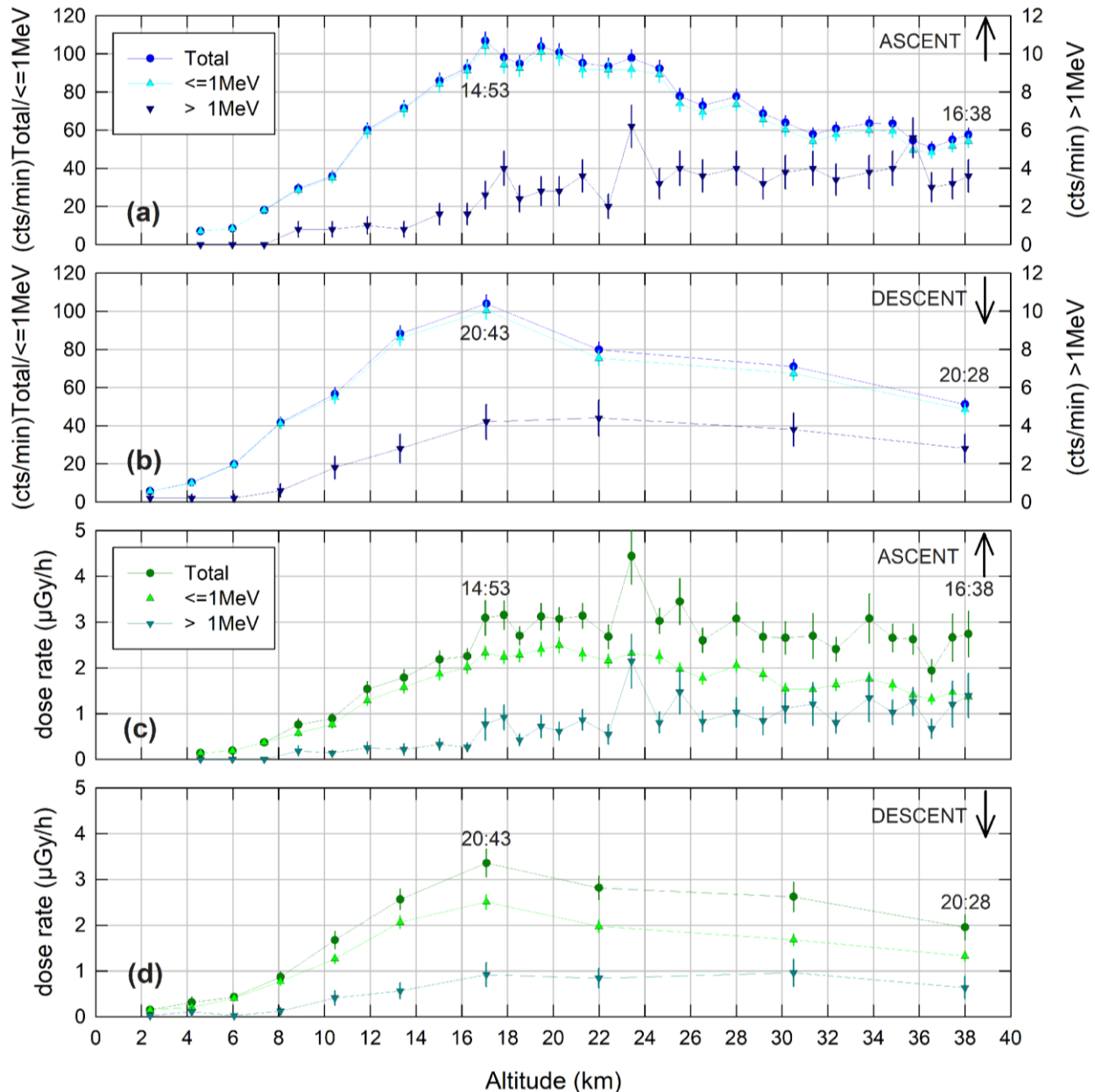


660 Figure 14. MARSBOx energy deposition spectra over the full New Mexico mission (for energy
 661 depositions $E_{Dep} \leq 1$ MeV in Si).
 662
 663

664 To further illustrate and investigate the Regener maxima, Figure 14 presents the energy
 665 deposition spectra (limited to $E_{Dep} \leq 1$ MeV) across the full MARSBOx mission. Two clear

666 peaks at the start (14:53 – 15:13 UTC) and at the end (20:43 UTC) of the mission were
 667 noteworthy. The peaks appear only in the lowest energy deposition channels for MARSBOx up
 668 to ~400 keV, indicating that the dominant source in the low energy regimes was electrons (see
 669 also calculations for the count rate in Figure 11 a).

670 First, we will focus on comparing the count- and dose rate profiles for the slow ascent
 671 and the fast descent of MARSBOx, partitioned as total energy deposition spectra plus the
 672 relevant cuts for low energies ($E_{Dep} \leq 1\text{MeV}$) and high energies ($E_{Dep} > 1\text{MeV}$).



673
 674 Figure 15. Count- and dose rate versus altitude for MARSBOx over New Mexico: (a) total count
 675 rate and count rate for energy regimes $E_{Dep} \leq 1\text{ MeV}$ and $E_{Dep} > 1\text{ MeV}$ for the ascent of the
 676 balloon (b) same data for the descent; (c) total dose rate and dose rate for energy regimes
 677 $E_{Dep} \leq 1\text{ MeV}$ and $E_{Dep} > 1\text{ MeV}$ for the ascent of the balloon (b) same data for the descent.
 678

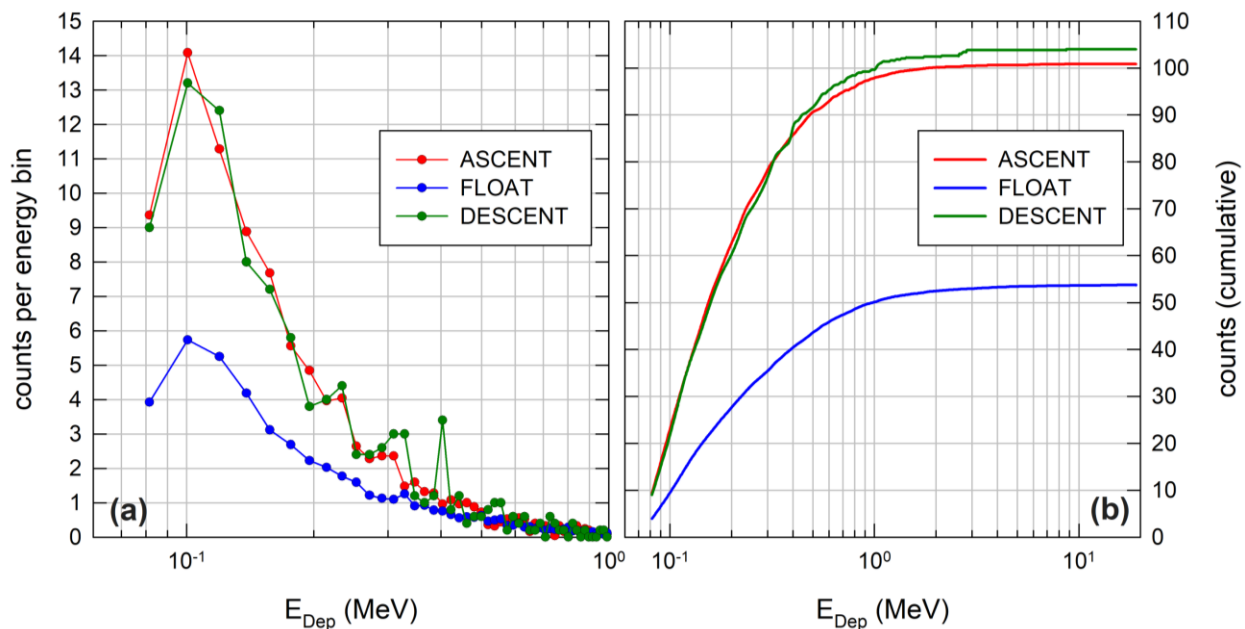
679 The relevant ascent data are provided in Figure 15a and Figure 15c, showing the count-
 680 and dose rates up to float altitude at around 16:30 UTC. The descent data are displayed in Figure
 681 15b and Figure 15d, again with count- and dose rate values for the payload starting ~38 km
 682 altitude at 20:28 UTC.

683 During ascent, the first maximum in count rates was reached at 14:53 UTC at an altitude
 684 of 17.02 km. This maximum was also seen in the dose rates, at least up to 15:13 UTC, where the
 685 maxima remained both in count- and dose rates, and then slowly declined until a stable float
 686 altitude. Averaging across five data points (from 14:53 – 15:13 UTC) with altitudes ranging from
 687 17.02 to 20.26 km yielded a count rate of 101 ± 2 cts/min and dose rate of 3.0 ± 0.4 μ Gy/h.

688 During the descent of the balloon carrying MARSBOx, the M-42 instrument reached its
 689 maximum of count- and dose rates at 20:43 UTC, with a count rate of 107 ± 5 cts/min and a
 690 respective dose rate of 3.3 ± 0.4 μ Gy/h. In comparison to ascent and descent data, the average
 691 dose rate for the mission’s float altitude was 2.5 ± 0.4 μ Gy/h with an average count rate of
 692 54 ± 1 cts/min (see also Table 2).

693 Based on results for the fluence rate presented earlier in Figure 11a, and to generate a
 694 comparison of the possible changes in the energy deposition spectra over the mission phases, we
 695 can go even further by looking at three distinct flight locations (ascent, float, descent), as
 696 summarized in Figure 16. With Figure 16a, the averaged spectra for ascent (from 14:53 – 15:13
 697 UTC), float (from 17:00 – 20:00 UTC) and descent (20:43 UTC) were depicted. Next, Figure
 698 16b compares the cumulative count rate for ascent, float and descent.

699



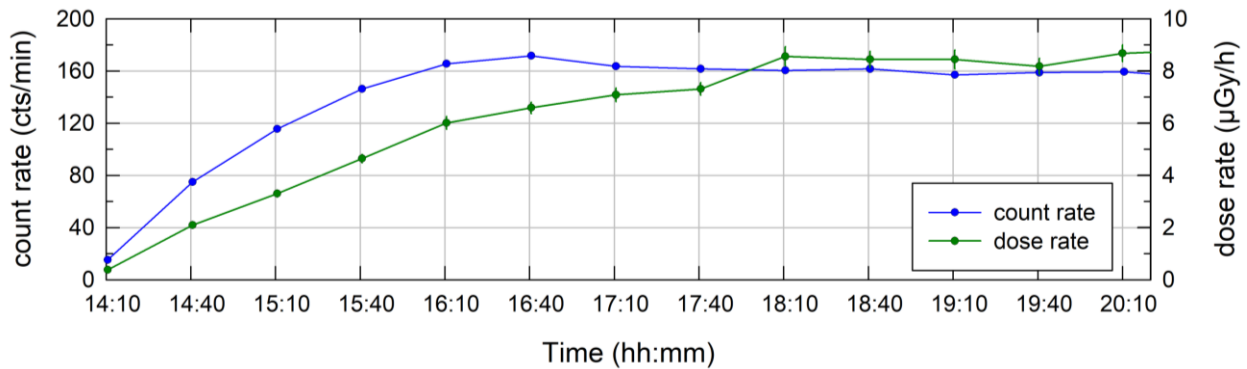
700 Figure 16. (a) MARSBOx energy deposition spectra (limited to $E_{Dep} \leq 1$ MeV) for the ascent,
 701 float and descent of the mission; (b) cumulative counts for ascent, float and descent.
 702

703
 704 The peak in energy depositions at ~100 keV for both ascent and descent profiles in
 705 Figure 16a was striking in comparison to the data at float altitudes and can be related to the peak
 706 in electrons at this altitude (see Figure 11a). Even though we only have one data point (20:43
 707 UTC) for the descent of the balloon, the values seemed to mirror the ascent, thereby showing
 708 where the Regener Maximum crossing occurred. By focusing on the cumulative counts, overlap

709 between ascent and descent can be noted, with a clear distinction compared to the float altitude.
 710 For instance, the counts beneath and above 1 MeV were nearly the same for ascent and descent
 711 ($97\% \leq 1\text{MeV}$ and $3\% > 1\text{MeV}$), but changed to $93\% \leq 1\text{MeV}$ and $7\% > 1\text{MeV}$ at float altitudes.
 712 Together, this showed the difference between energy deposition spectra during the MARSBox
 713 mission and the clear distinction, which can be made to quantify the Regener maximum, standing
 714 out from results measured at float altitude.

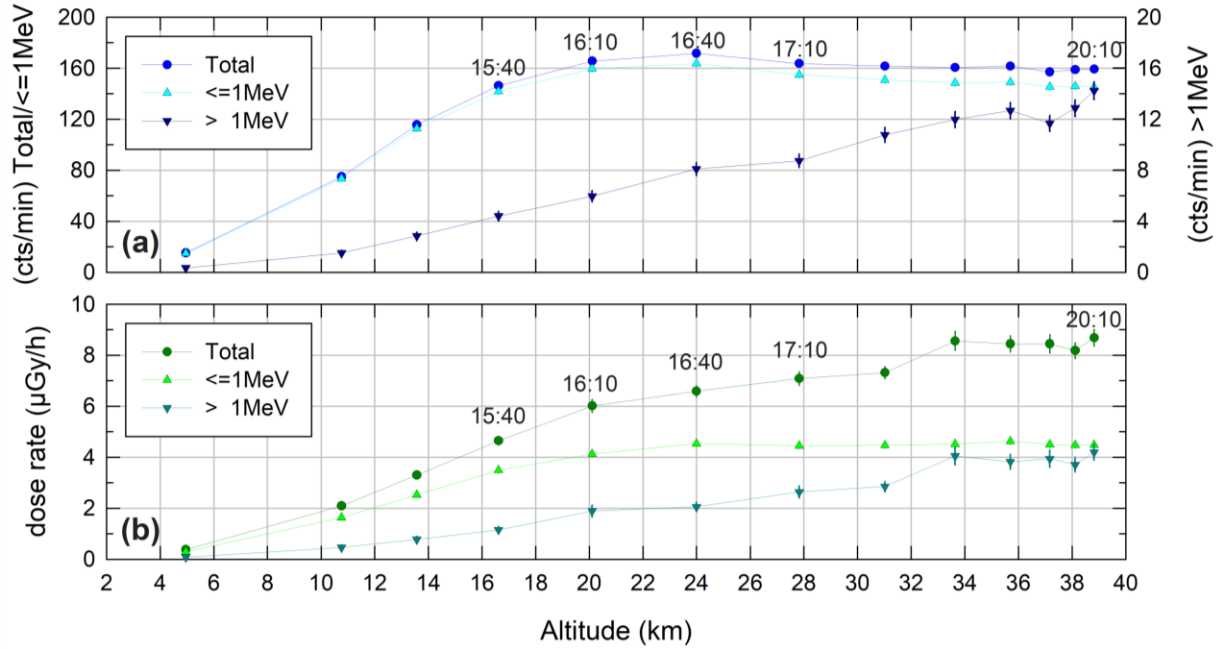
715 4.5.2. E-MIST - ascent

716 In this section, we analyze the conditions during E-MIST ascent. Pertinent count- and
 717 dose rate data from launch upon reaching the ~ 39 km float altitude is provided in Figure 17. Data
 718 acquisition started at 13:55 UTC with the middle of a 30-minute integration interval for the M-42
 719 detector at 14:10 UTC. From there (14:10 up to 20:10 UTC), the count rate profile increased,
 720 reaching a maximum at 16:40 UTC (172 ± 2 cts/min), and, finally, started a decrease with values
 721 at 20:10 UTC of 159 ± 2 cts/min. Unlike the count rate, the dose rate slowly increased over the
 722 entire duration of the ascent. These result will be explored in Figure 18 and the discussion below.
 723



724
 725 Figure 17. E-MIST over Antarctica during the 6-hour ascent of the balloon: count rate (cts/min);
 726 dose rate ($\mu\text{Gy/h}$).
 727

728 Figure 18a and Figure 18b reveal the dependence on altitude for the total energy
 729 deposition spectra and at regimes $E_{Dep} \leq$ and $E_{Dep} > 1$ MeV, for count- and dose rate,
 730 respectively. Looking at 4 specific times from 15:40 to 17:10 UTC, can help illustrate the
 731 pattern. The maximum in total count rate occurred at 16:40 UTC, also observed for the low
 732 energy cut; while the count rate for the high energy cut > 1 MeV increased steadily upon
 733 reaching the final float altitude. Meanwhile, for the dose rate profiles (Figure 18b), values
 734 increased upon reaching float altitude, while the dose rate for ≤ 1 MeV already reached a plateau
 735 at 24 km (16:40 UTC). The dose rate profile for the energy regime $> 1\text{MeV}$ flattened out around
 736 34 km (18:10 UTC). Table 4 compiles count- and dose rate data for the aforementioned time
 737 periods.
 738
 739
 740
 741
 742



743
744

745 Figure 18. E-MIST: (a) total count rate and count rate for energy regimes $E_{Dep} \leq$ and $E_{Dep} > 1$
746 MeV for the ascent of the balloon; (b) total dose rate and dose rate for energy regimes $E_{Dep} \leq$ and
747 $E_{Dep} > 1$ MeV for the ascent of the balloon.

748
749

Table 4

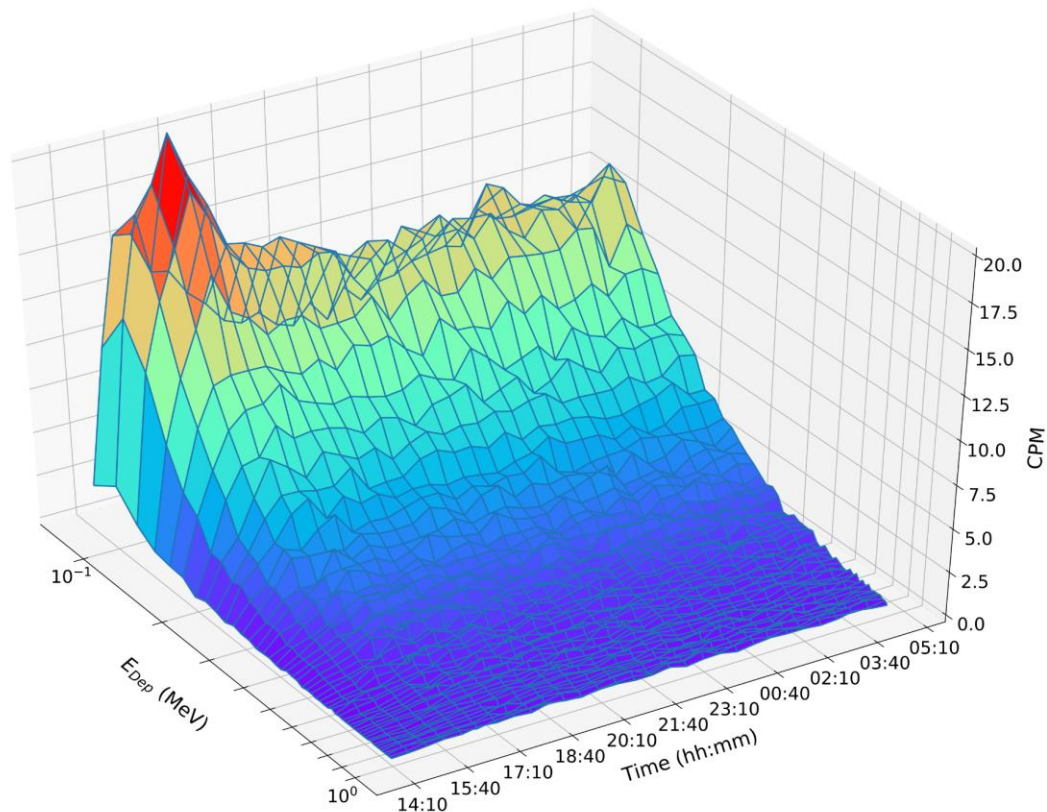
750 *Count rate and dose rate data for the Regener maximum plus data for float altitude for E-MIST*

		Time (hh:mm) (UTC)				
		15:40	16:10	16:40	17:10	20:10 (float)
Altitude	km	16.62	20.11	23.99	27.82	38.82
Altitude range	km	14.99 – 18.13	18.13 – 21.89	21.89 – 26.10	26.10 – 29.61	38.46 – 39.11
Count rate	Total	146±2	166±2	172±2	164±2	159±2
	≤1MeV	142±2	160±2	164±2	155±2	145±2
	>1MeV	4±0.40	6±0.45	8±0.52	9±0.55	14±0.70
Count rate (%)	≤1MeV	97.0	96.4	95.3	94.7	91.1
	>1MeV	3.0	3.6	4.7	5.3	8.9
Dose rate	Total	4.6±0.2	6.0±0.3	6.6±0.2	7.1±0.3	8.7±0.3
	≤1MeV	3.5±0.1	4.1±0.1	4.5±0.1	4.4±0.1	4.5±0.1
	>1MeV	1.2±0.1	1.9±0.2	2.1±0.2	2.6±0.2	4.2±0.3
Dose rate (%)	≤1MeV	75.1	68.6	68.8	62.8	51.7
	>1MeV	24.9	31.4	31.2	37.2	48.3

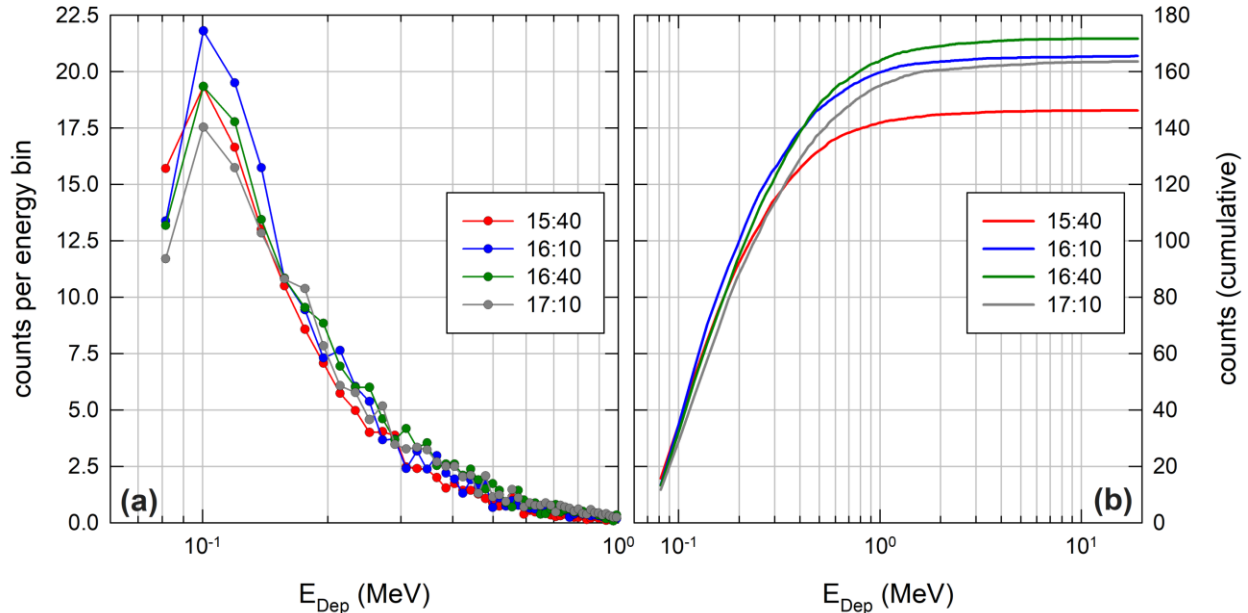
751
752
753

The count- and dose rate data from when the payload reached float at 20:10 UTC are of special significance and were also included in Table 4 for comparison. At 16:40 UTC, around

754 95% of the count rate was for energy depositions ≤ 1 MeV. This value decreased to 91% at float
 755 altitude, indicating that the spectra itself changed, hardening for the higher altitudes. A similar
 756 behavior was observed for the dose percentage. At 16:40 UTC, only 31% of the dose was from
 757 energy depositions > 1 MeV, and the value rose to 48 % at float altitude, again indicating harder
 758 spectral conditions. We also noticed the pattern for MARSBOx mission values, where at float it
 759 was a 42% dose contribution from high energy depositions. Taken together, and when applied to
 760 E-MIST over Antarctica, we can conclude the balloon reached its Regener maximum in count
 761 rates at 16:40 UTC with an altitude of ~ 24 km (the exact altitude range over the 30-minute
 762 integration period was 21.89 – 26.10 km). But we must also consider the different parts of the
 763 energy deposition spectra to determine if E-MIST crossed the maximum at this point during the
 764 mission, and not rely solely upon the total count rate for this interval (with the detector
 765 measuring energy depositions up to 20 MeV in Si). So, in Figure 19 we provide a three-
 766 dimensional energy deposition spectrum limited to $E_{Dep} \leq 1$ MeV for the first 15 hours of the
 767 mission (similar to Figure 14 for MARSBOx). With this approach, the peak of counts in the
 768 lowest energy regime, shortly after the start of the mission, was readily identifiable. Moreover,
 769 the lower energy deposition regime (up to 200 keV in Si) flattened out and then stayed relatively
 770 constant at float altitudes and onward during the mission.
 771



772 Figure 19. E-MIST energy deposition spectra for first 15 hours of the Antarctic flight during
 773 balloon ascent (for energy depositions $E_{Dep} \leq 1$ MeV in Si).
 774
 775



776
777

778 Figure 20. (a) Energy distribution and cumulative counts for 4 distinct time periods of E-MIST
779 float (limited $E_{Dep} \leq \text{MeV}$ in Si); (b) cumulative counts.

780

781 After applying this refined focus, we now see a peak closer to 16:10 UTC with the
782 balloon altitude of 20.11 km (altitude range 18.13 – 21.89 km); rather different from the earlier
783 identified peak at 16:40 UTC when only the total count rates were considered. To further
784 investigate this peak, we examined the energy deposition spectra for the four periods of interest
785 (15:40 – 17:10 UTC) in Figure 20a, with Figure 20b showing the cumulative count integrated
786 over the whole energy range of the spectra. Yet again as with Figure 16 for MARSBOX, Figure
787 20 showing the peak at 16:10 UTC consistent with the 3D spectra (Figure 19), and we observe
788 the peak of electrons in the relevant altitude range as flown through at 16:10 UTC consistent
789 with the calculated count rate profile (Figure 11b).

790 Considering this pattern we can conclude another maximum of count rates was reached
791 (in the lowest energy channels) at 16:10 UTC due to the electron contributions during ascent of
792 the balloon, even though the maximum of the total count rate was reached at 16:40 UTC for the
793 whole energy range of the M-42 instrument. Our assertion is supported by Figure 20b, where the
794 cumulative count rates at 16:10 UTC were at maximum, but only up
795 to ~ 400 keV. From this energy deposition point onward to 16:40 UTC the instrument yielded
796 maximum count rates of 172 ± 2 cts/min.

797 5. Summary and Conclusion

798 With two consecutively-flown, high altitude balloon mission observations within a four-
799 month timeframe (23 September 2019 to 12 January 2020) from New Mexico and Antarctica, we
800 demonstrated it is realistic to obtain robust radiation environmental data by using a small,
801 simple-to-integrate radiation detector system (M-42). Our results provide, for the first time, a
802 direct comparison of mid-latitude and polar stratosphere radiation conditions in a region of the

803 Earth's atmosphere that remained largely uncharacterized to date. The similarities and
804 differences in GCR at these disparate locations set the stage for refining future measurements
805 while validating Geant4 model predictions. We observed a cut-off rigidity for MARSBOx over
806 New Mexico of around 3.95 GV, whereas E-MIST over Antarctica results ranged from 0 GV up
807 to 1.4 GV during the stratospheric circumnavigation of the continent. Our data showed a clear
808 dependency of count- and dose rates based on: (a) the site of the flights; (b) the cut-off rigidity
809 comparing the two flights; and (c) the changes in cut-off rigidity for conditions over Antarctica.
810 With the mid-latitude, relatively short-lasting New Mexico flight, average dose values were
811 2.5 ± 0.4 $\mu\text{Gy/h}$. In sharp contrast, Antarctic average dose values were much higher, reaching
812 8.4 ± 0.3 $\mu\text{G/h}$ at 0 GV cut-off rigidity. With the New Mexico mission, our count rate and the
813 dose rate datasets displayed a crossing of the Regener Maximum during both ascent and descent
814 between 17.5 and 20 km. By comparison, the Antarctic datasets included a Regener maximum
815 only in count rates at an altitude of 24 km, but not in the measured dose rate. The values for
816 measured data remained within the error bars of our Geant4 simulation, with the strongest
817 alignment during Antarctic float altitudes and deviations that could be corrected by adjusting to
818 known limits of the energy deposition regime for the M-42 detector. The maximum measured
819 daily dose values over Antarctica reached 202 $\mu\text{Gy/day}$ (at $R_C = 0$ GV), a level of particular
820 significance for the space exploration community, considering we have observed similar dose
821 values (212 $\mu\text{Gy/day}$) on the surface of Mars across equivalent time periods, as measured by the
822 Curiosity rover (Berger et al., 2020). Short of sending experiments or instruments to the Red
823 Planet, or as a progressive stepping stone for eventually journeying into deep space, our
824 dosimetry results support the idea that long duration Antarctic balloon missions can be used for
825 accurately introducing experiments or instruments to sustained Mars-like radiation conditions.

826
827
828
829
830
831
832
833
834
835
836
837
838
839
840
841
842
843
844
845
846
847

848 **Appendix A: E-MIST**

849 Within this appendix we provide additional figures for the E-MIST mission.
850



851
852
853
854
855
856

Figure A1. The SuperTIGER-2.3 balloon mission payload carrying E-MIST and the M-42 detector, shortly before launch from Antarctica on 15 December 2019 (*red box* around E-MIST payload with the M-42 detector) © NASA



857
858
859
860
861
862
863
864
865
866
867

Figure A2. The SuperTIGER-2.3 balloon mission (*red box* around the E-MIST payload with the M-42 detector). Picture was taken during the payload recovery operation after landing on the Antarctic ice shelf, following the 32-day mission in the polar stratosphere. © NASA

868 In the following section, we provide additional graphical representations of the data for the E-
869 MIST mission as 2D plots following the mission trajectory of the E-MIST mission.

870

871 Figure A3 shows the 2D plot for the timeline of the mission.

872

873 Figure A4 shows the 2D plot for the calculated cut-off rigidity (R_C).

874

875 Figure A5 shows the 2D plot for the measured count rates (*clean + interpolated*).

876

877 Figure A6 shows the 2D plot for the measured dose rates (*clean + interpolated*).

878

879 Figure A7 shows the 2D plot for the calculated dose rates applying the correction factor (*cf*).

880

881 Figure A8 shows the 2D plot for the calculated dose rates.

882

883

884

885

886

887

888

889

890

891

892

893

894

895

896

897

898

899

900

901

902

903

904

905

906

907

908

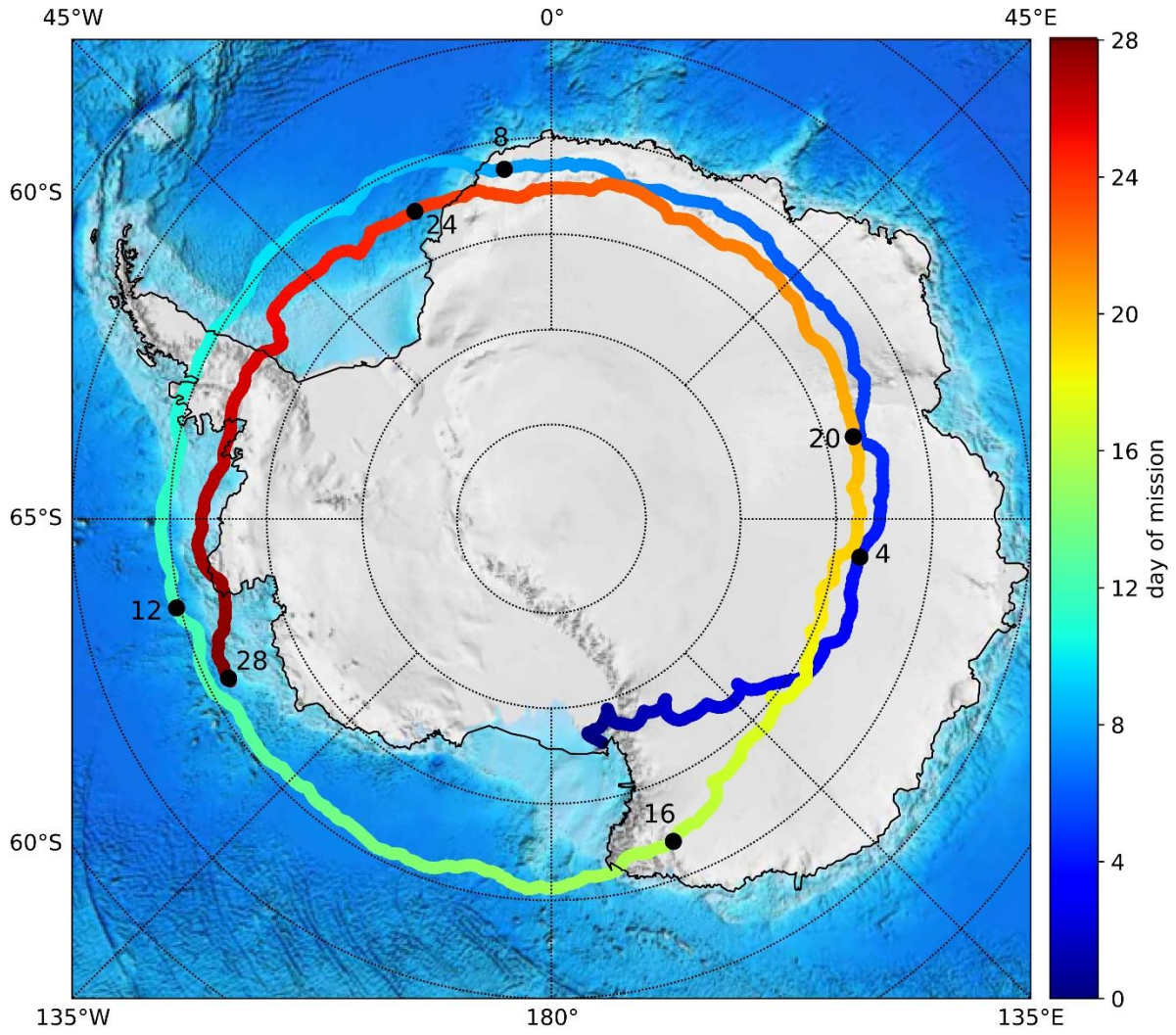
909

910

911

912

913



914
915
916
917
918
919
920
921
922
923
924
925
926
927
928
929
930
931

Figure A3. The E-MIST flight profile.

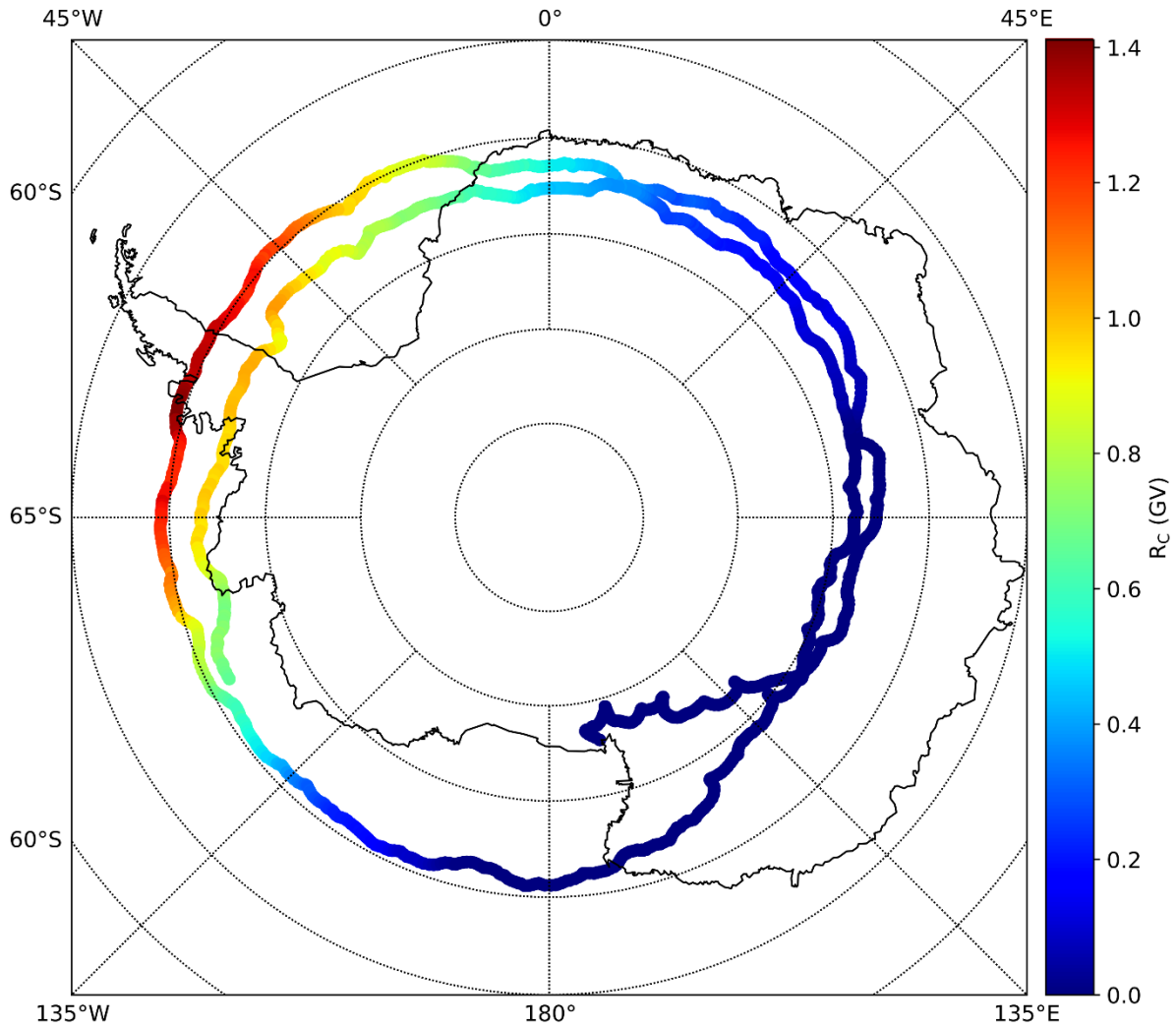
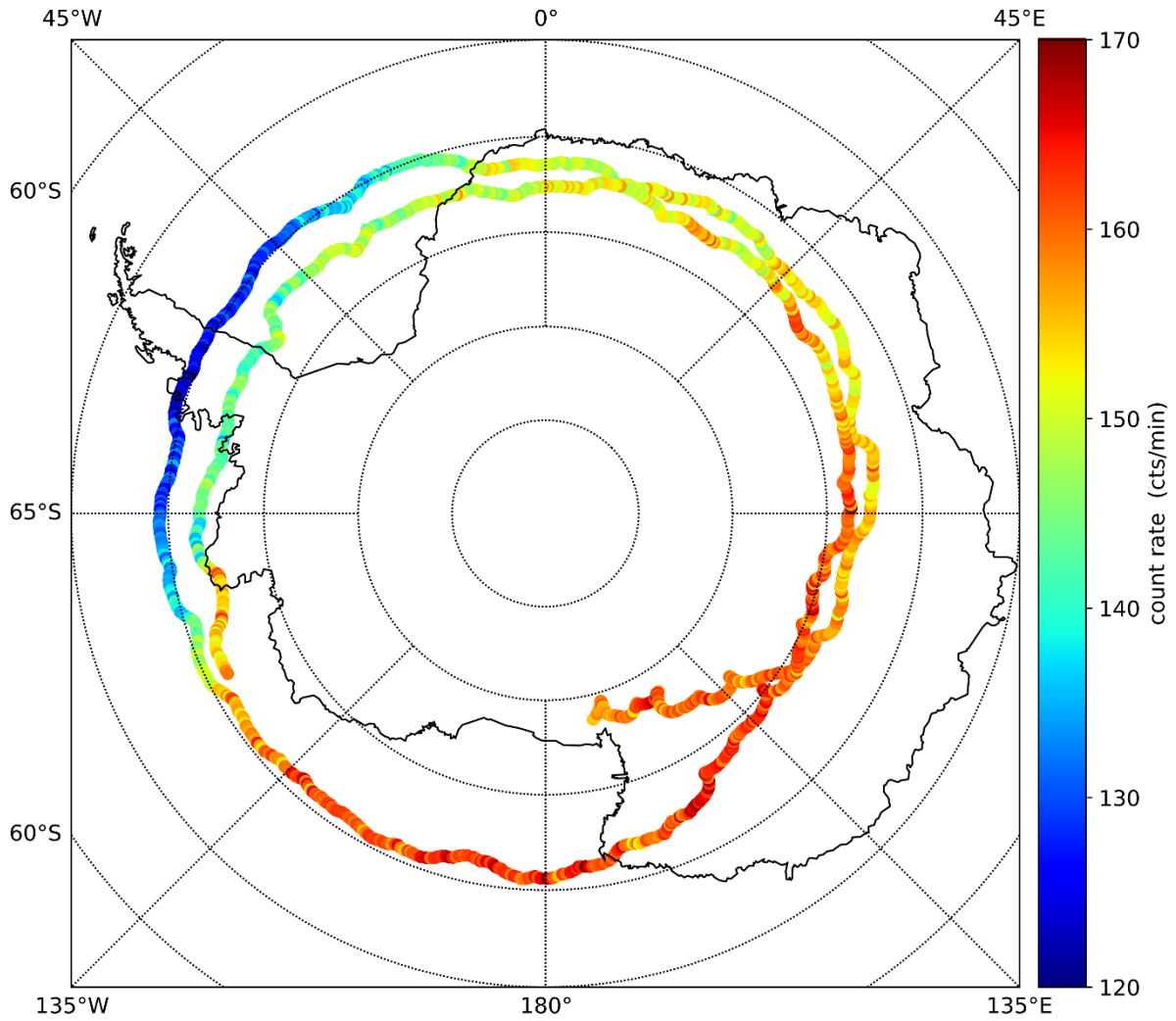


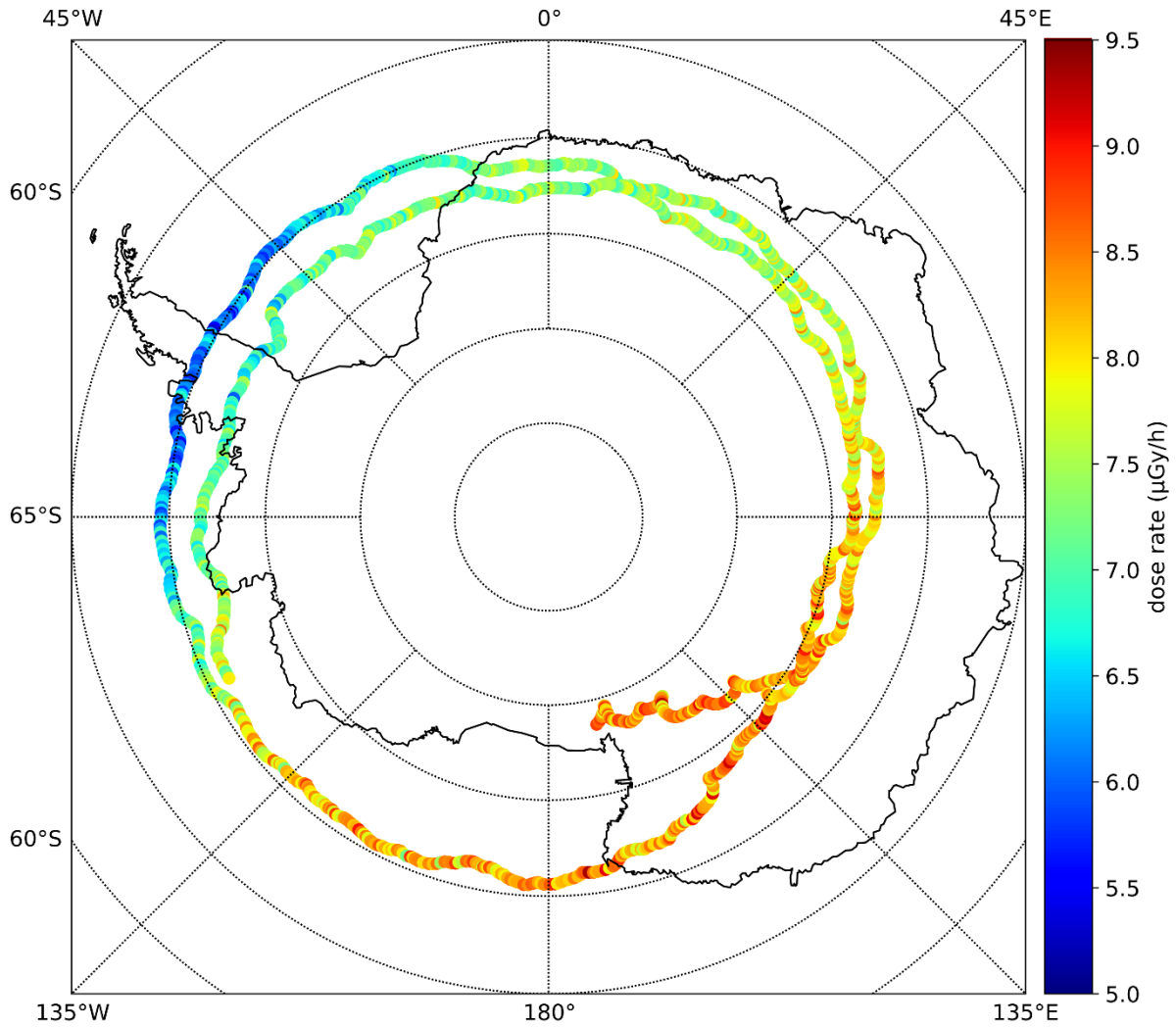
Figure A4. The cut-off rigidity (R_c) over the E-MIST mission.

932
933
934
935
936
937
938
939
940
941
942
943
944
945
946
947
948
949
950



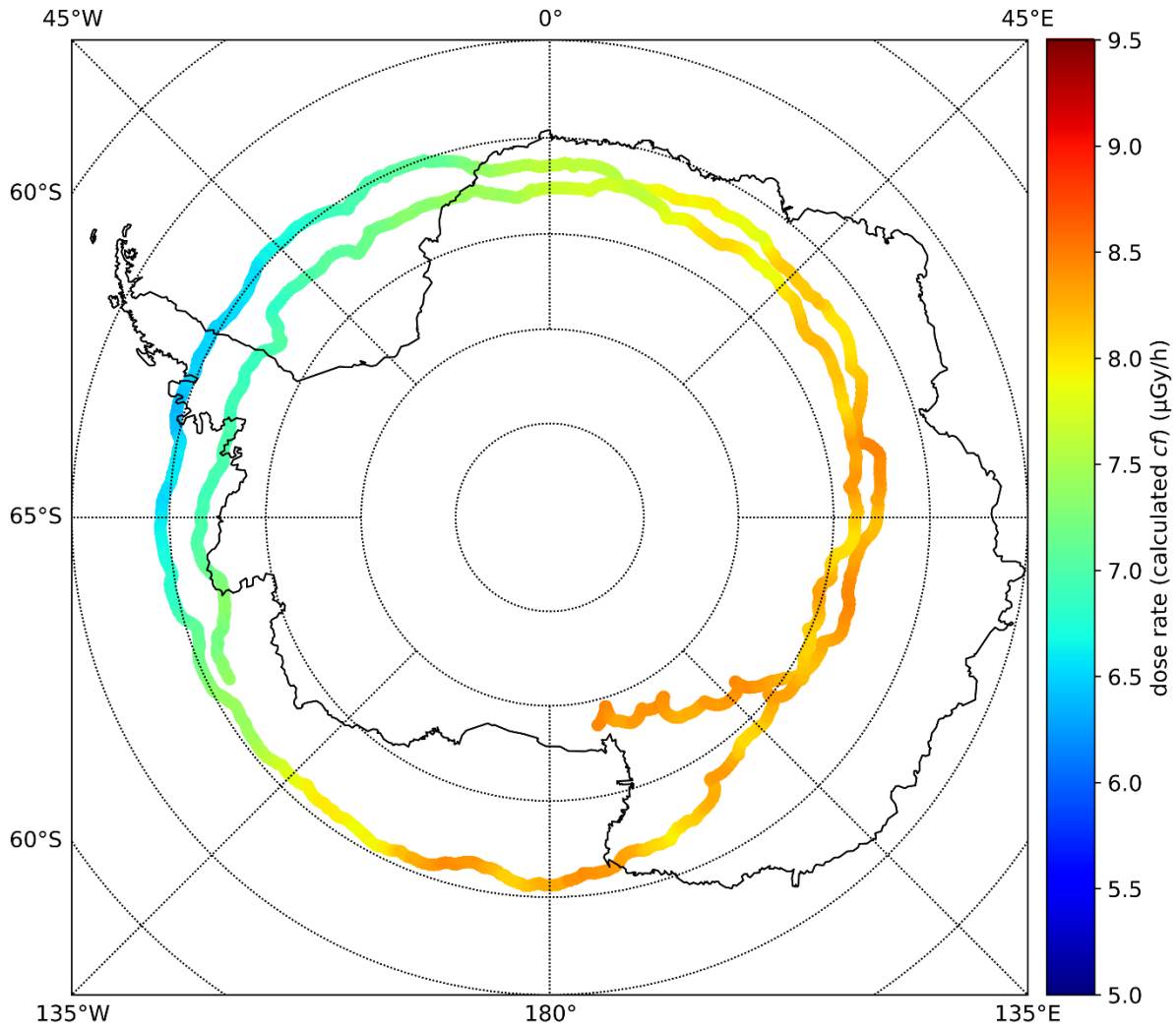
951
 952
 953
 954
 955
 956
 957
 958
 959
 960
 961
 962
 963
 964
 965
 966
 967
 968

Figure A5. The measured count rate profile (cts/min) over the E-MIST mission. Note: Data refers to the *clean + interpolated* count rate profile as given in Figure 6e.



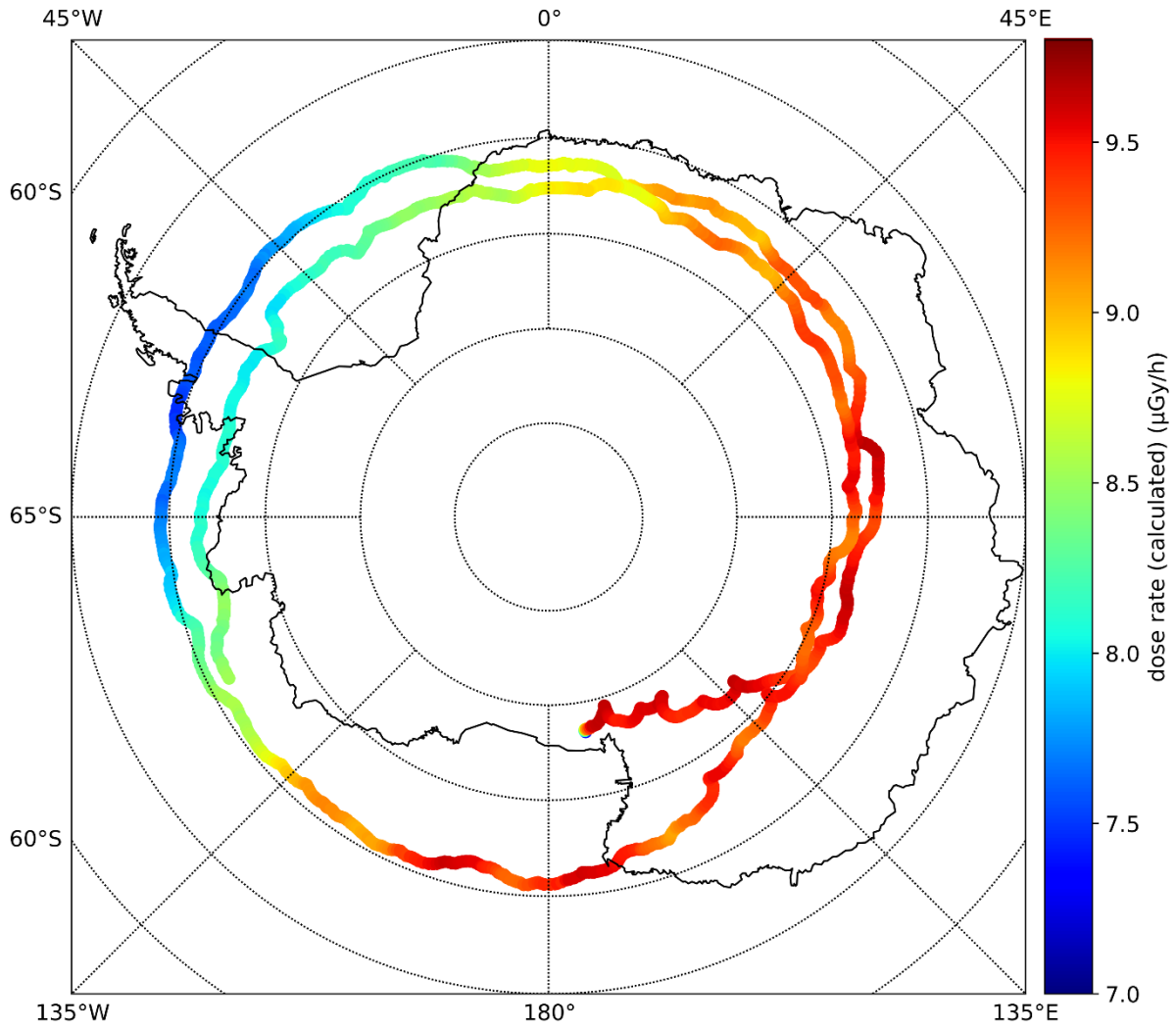
969
 970
 971
 972
 973
 974
 975
 976
 977
 978
 979
 980
 981
 982
 983
 984
 985
 986

Figure A6. The measured dose rate profile ($\mu\text{Gy/h}$) for the E-MIST mission. Note: Data refers to the *clean + interpolated* dose rate profile as given in Figure 6f and Figure 13b.



987
 988
 989
 990
 991
 992
 993
 994
 995
 996
 997
 998
 999
 1000
 1001
 1002
 1003
 1004

Figure A7. The simulated dose rate profile ($\mu\text{Gy/h}$) for the E-MIST mission with the applied correction factors (cf) for R_C and altitude dependence as given in Figure 13b (orange dotted line). Note: Data shown for comparison with the measured dose rate data as given in Figure A6.



1005
 1006
 1007
 1008
 1009
 1010
 1011
 1012
 1013
 1014
 1015
 1016
 1017
 1018
 1019
 1020
 1021
 1022
 1023

Figure A8. The simulated dose rate profile ($\mu\text{Gy/h}$) for the E-MIST mission as given in Figure 13b (orange dashed line).

1024 **Acknowledgments**

1025 At DLR, Cologne, DLR M-42 was supported by the DLR grant FuE-Projekt
1026 | “OrionRAD” (Programm RF-FuW, Teilprogramm 475).

1027 We would like to thank the NASA Balloon Program Office (BPO), Wallops Flight
1028 Facility (WFF), and the staff at the Columbia Scientific Balloon Facility (CSBF), especially
1029 Chris Field, Robert Salter and Hugo Franco for flight activities from Fort Sumner, New Mexico,
1030 and Antarctica. For the Antarctic mission, our experiment was enabled through the generosity of
1031 the SuperTIGER-2.3 team at Washington University in St. Louis (WUSTL); in particular, we
1032 express gratitude to Richard Bose, Dana Braun, and Garry Simburger. SuperTIGER-2.3 was
1033 funded by NASA grants NNX15AC23G and 80NSSC20K0405. Extensive logistical support for
1034 the polar mission was provided by a NASA/National Science Foundation (NSF) agreement
1035 supporting awards A-454-M and A-142-M through the United States Antarctic Program’s
1036 Antarctic Support Contractor (ASC) at the Long-Duration Balloon (LDB) Facility. We wish to
1037 thank Kaija Webster and Scott Battaion (CSBF) from ASC for arranging Antarctic mission
1038 activities including post-flight recovery. NASA payloads and team members described herein
1039 were funded through balloon research grants from NASA Planetary Protection Research (PPR)
1040 and NASA Space Biology.

1041 **Data Availability Statement**

1042 The data for the sun spot number was obtained from <http://www.sidc.be/silso/>. Oulu
1043 Neutron Monitor (NM) count rate data is provided at <https://cosmicrays oulu.fi/>. The values of
1044 the Kp index were retrieved from <ftp://ftp.gfz-potsdam.de/pub/home/obs/kp-ap/>. ACE data was
1045 retrieved from <ftp://ftp.swpc.noaa.gov/pub/lists/ace/>.

1046
1047 For the purpose of peer review the data used to generate all figures within the manuscript
1048 is provided under the following link for download:

1049 <https://gigamove.rz.rwth-aachen.de/d/id/YpD8GDJpNVxRD?20&id=YpD8GDJpNVxRD>

1050
1051 For the purpose of peer review the data used to generate the animated movies within the
1052 supplementary material is provided under the following link for download:

1053 <https://gigamove.rz.rwth-aachen.de/d/id/ELnt5HjgpJKMe6?24&id=ELnt5HjgpJKMe6>

1054
1055 Data used to generate all figures and movies of the supplementary material within the
1056 manuscript will be made available under the DLR repository at <https://zenodo.org>.

1057
1058
1059
1060
1061
1062
1063
1064
1065

1066 **References**

- 1067 Agostinelli, S., Allison, J., Amako, K. A., Apostolakis, J., Araujo, H. et al. (2003). GEANT4-a
 1068 simulation toolkit. *Nuclear Instruments and Methods in Physics Research Section A: Accelerators Spectrometers Detectors and Associated Equipment*, 506(3), 250-303.
 1069 [https://doi.org/10.1016/S0168-9002\(03\)01368-8](https://doi.org/10.1016/S0168-9002(03)01368-8)
 1070
- 1071 Allison, J., Amako, K., Apostolakis, J. E. A., Araujo, H., Dubois, P., Asai, M., et al. (2006).
 1072 Geant4 developments and applications. *IEEE Transactions on Nuclear Science*, 53, 270-278.
 1073 <https://doi.org/10.1109/TNS.2006.869826>
 1074
- 1075 Allison, J., Amako, K., Apostolakis, J., Arce, P., Asai, M., et al. (2016). Recent developments in
 1076 GEANT4. *Nuclear Instruments and Methods in Physics Research Section A: Accelerators Spectrometers Detectors and Associated Equipment*, 835, 186-225.
 1077 <https://doi.org/10.1016/j.nima.2016.06.125>
 1078
- 1079 Bellotti, R., Cafagna, F., Circella, M., De Marzo, C. N., Golden, R. L., Stochaj, S. J. et al.
 1080 (1999). Balloon measurements of cosmic ray muon spectra in the atmosphere along with those of
 1081 primary protons and helium nuclei over midlatitude. *Physical Review D*, 60(5), 052002.
 1082 <https://doi.org/10.1103/PhysRevD.60.052002>
 1083
- 1084 Berger, T., Marsalek, K., Aeckerlein, J., Hauslage, J., Matthiä, D., Przybyla, B. et al. (2019). The
 1085 German Aerospace Center M-42 radiation detector – a new development for applications in
 1086 mixed radiation fields. *Review of Scientific Instruments*, 90, 125115.
 1087 <https://doi.org/10.1063/1.5122301>
 1088
- 1089 Berger, T., Matthiä, D., Burmeister, S., Zeitlin, C., Rios, R., Stoffle, N. et al. (2020). Long term
 1090 variations of galactic cosmic radiation on board the International Space Station, on the Moon and
 1091 on the surface of Mars. *Journal of Space Weather and Space Climate*, 10, 34.
 1092 <https://doi.org/10.1051/swsc/2020028>
 1093
- 1094 Binns, W.R., Bose, R.G., Braun, D.L., Brandt, T.J., Daniels, W.M., De Nolfo, G.A. et al. (2013).
 1095 *The Super-TIGER Experiment*. Paper presented at the 33rd International Cosmic Ray Conference,
 1096 02 – 09 July, 2013, Rio de Janeiro, Brasil. Retrieved from:
 1097 <https://galprop.stanford.edu/elibrary/icrc/2013/papers/icrc2013-0645.pdf>
 1098
- 1099 Boezio, M., Carlson, P., Francke, T., Weber, N., Suffert, M., Hof, M., et al. (1999). The Cosmic-
 1100 Ray Proton and Helium Spectra between 0.4 and 200 GV. *The Astrophysical Journal*, 518(1),
 1101 457-472. <https://doi.org/10.1086/307251>
 1102
- 1103 Boezio, M., Carlson, P., Francke, T., Weber, N., Suffert, M., Hof, M. et al. (2000). The cosmic-
 1104 ray electron and positron spectra measured at 1 AU during solar minimum activity. *The Astrophysical Journal*, 532(1), 653. <https://doi.org/10.1086/308545/>
 1105
- 1106 Carlson, P., & Watson, A.A. (2014). Erich Regener and the ionization maximum of the
 1107 atmosphere. *History of Geo- and Space Sciences*, 5, 175-182. <https://doi.org/10.5194/hgss-5-175-2014>
 1108
- 1109
 1110
 1111

- 1112
 1113 Carmichael, H., & Dymond, E. G. (1939). High altitude cosmic radiation measurements near the
 1114 north geomagnetic pole. *Proceedings of the Royal Society A*, 171(946), 321-344.
 1115 <https://doi.org/10.1098/rspa.1939.0069>
 1116
- 1117 Cortesão, M., Siems, L., Koch, S., Beblo-Vranesevic, K., Rabbow, E., Berger, T. et al. (2020).
 1118 MARSBOX: Fungal and bacterial endurance from a balloon-flown analog mission in the
 1119 stratosphere. *Frontiers in Microbiology*, 12, 601713. <https://doi.org/10.3389/fmicb.2021.601713>
 1120
- 1121 DuVernois, M. A., Barwick, S. W., Beatty, J. J., Bhattacharyya, A., Bower, C. R., Chaput, C. J.
 1122 et al. (2001). Cosmic-Ray Electrons and Positrons from 1 to 100 GeV: Measurements with
 1123 HEAT and Their Interpretation. *The Astrophysical Journal*, 559(1), 296-303.
 1124 <https://doi.org/10.1086/322324>
 1125
- 1126 Goldhagen, P., Clem, J., & Wilson, J. (2004). The energy spectrum of cosmic-ray induced
 1127 neutrons measured on an airplane over a wide range of altitude and latitude. *Radiation*
 1128 *Protection Dosimetry*, 110(1-4), 387-392. <https://doi.org/10.1093/rpd/nch216>
 1129
- 1130 Grieder, P. K. (2001). *Cosmic Rays at Earth*. Elsevier. 27 July 2001, ISBN 9780444507105
 1131
- 1132 Hams, T., Binns, W.R. Bose, R.G., Braun D.K, Brandt, T.J., Daniels, W.M., et al. (2016).
 1133 *SuperTIGER and the Origin of Galactic Cosmic Rays*. Paper presented at the 34th International
 1134 Cosmic Ray Conference, 30 July - 6 August, 2015, The Hague, The Netherlands.
 1135 <https://doi.org/10.22323/1.236.0435>
 1136
- 1137 Hands, A. D. P., Ryden, K.A. and C. J. Mertens C.J. (2016). The disappearance of the pfozter-
 1138 regener maximum in dose equivalent measurements in the stratosphere. *Space Weather*, 14, 776–
 1139 785. <https://doi.org/10.1002/2016SW001402>
 1140
- 1141 Hauslage, J., Strauch, S.M., Eßmann, O., Haag, F.W.M., Richter, P., Kruger, J., et al. (2018).
 1142 Eu:CROPIS – “*Euglena gracilis*: Combined Regenerative Organic-food Production in Space” -
 1143 A Space Experiment Testing Biological Life Support Systems Under Lunar And Martian
 1144 Gravity. *Microgravity-Science and Technology*, 30, 933-942. <https://doi.org/10.1007/s12217-018-9654-1>
 1145
- 1146
- 1147 Khodadad, C.L., Wong, G.M., James, L.M., Thakrar, P.J., Lane, M.A., Catechis, J.A., Smith,
 1148 D.J. (2017). Stratosphere conditions inactivate bacterial endospores from a Mars spacecraft
 1149 assembly facility. *Astrobiology*, 17(4), 337-350. <https://doi.org/10.1089/ast.2016.1549>
 1150
- 1151 Lowder, W. M., & Beck, H. L. (1966). Cosmic-ray ionization in the lower atmosphere. *Journal*
 1152 *of Geophysical Research* 71(19), 4661-4668. <https://doi.org/10.1029/JZ071i019p04661>
 1153
- 1154 Lowder, W. M., Zraft, P. D., & Beck, H. L. (1972). Experimental determination of cosmic ray
 1155 charged particle intensity profiles in the atmosphere. In: *Proceedings of the National Symposium*
 1156 *on Natural and Manmade Radiation in Space, Las Vegas, Nevada*. Retrieved from:
 1157 <https://ntrs.nasa.gov/api/citations/19720010073/downloads/19720010073.pdf>

- 1158
1159 Matthiä, D., Berger, T., Mrigakshi, A.I., and Reitz, G. (2013). A ready-to-use galactic cosmic ray
1160 model. *Advances in Space Research*, 51, 329-338. <https://doi.org/10.1016/j.asr.2012.09.022>
1161
- 1162 Matthiä, D., & Berger, T. (2017). The radiation environment on the surface of Mars – Numerical
1163 calculations of the galactic component with GEANT4/PLANETOCOSMICS. *Life Sciences in*
1164 *Space Research*, 14, 57-63. <https://doi.org/10.1016/j.lssr.2017.03.005>
1165
- 1166 Matthiä, D., Hassler, D. M., de Wet, W., Ehresmann, B., Firan, A., Flores-McLaughlin, J., et al.
1167 (2017). The radiation environment on the surface of Mars - Summary of model calculations and
1168 comparison to RAD data. *Life Sciences in Space Research*, 14, 18-28.
1169 <https://doi.org/10.1016/j.lssr.2017.06.003>
1170
- 1171 Meier, M. M., Matthiä, D., Forkert, T., Wirtz, M., Scheibinger, M., Hübel, R., and Mertens, C. J.
1172 (2016). RaD-X: Complementary measurements of dose rates at aviation altitudes. *Space*
1173 *Weather*, 14, 689-694. <https://doi.org/10.1002/2016SW001418>
1174
- 1175 Mertens, C. J. (2016). Overview of the Radiation Dosimetry Experiment (RaD-X) flight mission.
1176 *Space Weather*, 14, 921–934. <https://doi.org/10.1002/2016SW001399>
1177
- 1178 Mertens, C. J., Gronoff, G. P., Norman, R. B., Hayes, B. M., Lusby, T. C., Straume, T. et al.
1179 (2016). Cosmic radiation dose measurements from the RaD-X flight campaign. *Space Weather*,
1180 14, 874–898. <https://doi.org/10.1002/2016SW001407>
1181
- 1182 Norman, R. B., C. J. Mertens, and T. C. Slaba (2016). Evaluating galactic cosmic ray
1183 environment models using RaD-X flight data. *Space Weather*, 14, 764–775.
1184 <https://doi.org/10.1002/2016SW001401>
1185
- 1186 Neher, H. V. (1958). The Primary Cosmic Radiation. *Annual Review of Nuclear and Particle*
1187 *Science*, 8(1), 217-242. <https://doi.org/10.1146/annurev.ns.08.120158.001245>
1188
- 1189 Neher, H. V. (1971). Cosmic rays at high latitudes and altitudes covering four solar maxima.
1190 *Journal of Geophysical Research*, 76(7), 1637-1651. <https://doi.org/10.1029/JA076i007p01637>
1191
- 1192 Picone, J. M., Hedin, A. E., Drob, D. P., and Aikin, A. C. (2002). NRLMSISE-00 empirical
1193 model of the atmosphere: Statistical comparisons and scientific issues. *Journal of Geophysical*
1194 *Research*, 107, A12, 1468. <https://doi.org/10.1029/2002ja009430>
1195
- 1196 Rauch, B. F., Bose, R. G., West, A. T., Lisalda, T., Abarr, Q. et al. (2019). *SuperTIGER-2 2018*
1197 *Flight Payload Recovery and Preliminary Instrument Assessment*. Paper presented at 36th
1198 International Cosmic Ray Conference, 24 July – 01 August 2019, Madison, USA. Retrieved
1199 from: https://authors.library.caltech.edu/98062/1/ICRC2019_131.pdf
1200
- 1201 Regener, E., & Pfozter, G. (1935). Vertical Intensity of Cosmic Rays by Threefold Coincidences
1202 in the Stratosphere. *Nature*, 136, 718–719. <https://doi.org/10.1038/136718a0>
1203

1204
1205 Rosen, J. M., Hofmann, D. J., & Gringel, W. (1985). Measurements of ion mobility to 30 km.
1206 *Journal of Geophysical Research Atmospheres*, 90(D4), 5876-5884.
1207 <https://doi.org/10.1029/JD090iD04p05876>
1208
1209 Smith, D. J., Thakrar, P. J., Bharrat, A. E., Dokos, A. G., Kinney, T. L., James, L. M. et al.
1210 (2014). A balloon-based payload for Exposing Microorganisms in the Stratosphere (E-
1211 MIST). *Gravitational and Space Research* 2, 70–80.
1212
1213 Straume, T., Mertens, C.J., Lusby, T.C., Gersey, B., Tobiska, W.K., Norman, R.B. et al. (2016).
1214 Ground-based evaluation of dosimeters for NASA high-altitude balloon flight. *Space Weather*,
1215 14, 1011–1025. <https://doi.org/10.1002/2016SW001406>
1216
1217 Thébault, E., Finlay, C.C., Beggan, C.D., Alken, P., Aubert, J., Barrois, O., et al. (2015).
1218 International geomagnetic reference field: the 12th generation. *Earth, Planets and Space*, 67(1),
1219 79. <https://doi.org/10.1186/s40623-015-0228-9>
1220
1221 Zeitlin, C., Hassler, D., Ehresmann, B., Matthiä, D., Rafkin, S., Berger, T., et al. (2019).
1222 Measurements of Radiation Quality Factor on Mars with the Mars Science Laboratory Radiation
1223 Assessment Detector. *Life Sciences in Space Research*, 22, 89-97.
1224 <https://doi.org/10.1016/j.lssr.2019.07.010>
1225
1226 Zhang, S., Wimmer-Schweingruber, R.F., Yu, J., Wang, C., Fu, Q., Zou, Y. et al. (2020).
1227 First measurements of the radiation dose on the lunar surface. *Science Advances*, 6, eaaz1334.
1228 <https://doi.org/10.1126/sciadv.aaz1334>
1229
1230
1231
1232
1233
1234
1235
1236
1237
1238
1239
1240
1241
1242
1243
1244
1245
1246
1247
1248
1249

1250